Experimental and analytical study on the pre-crack impact response of thick multi-layered laminated glass under hard body impact

Xing-er Wang[a,b,e], Xuhao Huang[c*], Jian Yang[a,b,d], Xiaonan Hou[e], Yuhan Zhu[a,b], Dongdong Xie[a,b]

[a] State Key Laboratory of Ocean Engineering, Shanghai Jiao Tong University, Shanghai 200240, PR China

[b] Shanghai Key Laboratory for Digital Maintenance of Buildings and Infrastructure, School of Naval Architecture, Ocean and Civil Engineering, Shanghai Jiao Tong University, Shanghai 200240, PR China

[c] Key Laboratory of Impact and Safety Engineering, Ministry of Education， Faculty of Mechanical Engineering and Mechanics, Ningbo University, Ningbo, 315211, PR China

[d] School of Civil Engineering, University of Birmingham, Birmingham B15 2TT, UK

[e] Department of Engineering, Lancaster University, Lancaster, LA1 4YR, UK

Abstract: This study presents a combined experimental and analytical study on the impact response of multi-layered laminated glass (MLG) under low-velocity hard body impact before glass breakage. The drop weight impact tests using repeated attempts with increasing impact velocities were firstly performed on 12 MLG panels with double PVB or SG interlayers to record the impact response, high speed fracture process. The experimental results identify that: (1) the indentation is the predominant factor for glass fracture in the examined impact scenarios; (2) the key time interval of the pre-crack impact response is within 0.6 ms. The indentation which hasn't been considered in the existing analytical works was hence introduced into the proposed nonlinear analytical model, which employed third order shear deformation theory and obtained the solutions of motion equations by a two-step perturbation method, according to the former finding. The calculated impact response based on the proposed model was validated with the experimental results within 0.6 ms based on the latter finding and showed satisfactory agreement.

A parametric study was subsequently conducted to investigate the influence of factors such as the number of glass layers, glass thickness and ratio, panel size on the pre-crack impact response. The results show the increase of peak force and indentation is more sensitive to the increase of total glass thickness after the thickness reaches 24 mm and presents less sensitivity when the thickness approaches 57 mm. The variation of the glass thickness ratio has no influence on the pre-crack behavior once the total glass thickness is fixed.

Keywords: Laminated glass; Nonlinear dynamics; Structural glass; A two-step perturbation method; Hard body impact;

1. Introduction

1.1 Significance of glass elements under impact

Elements made of glass, e.g., glass windows, were classified as non-structural elements which were not designed to bear strong loads. This was mainly due to the limited applicability of early-stage glass products without adequate redundancy after glass fracture. In recent years, lamination with the high-performance polymeric interlayers such as plasticized polyvinyl butyral (PVB), SentryGlas® (SG) ionoplast interlayer facilitates the capability of glass products in the structural use. Emerging glass structures (e.g., Apple shops) using structural glass elements have been witnessed with a rapid increase of applications in the engineering practice, as it has the unique aesthetic and modern features due to the transparency of glass. Most of the glass products in the structural use adopt the laminated glass (LG), e.g., glass floor plate, staircase.

LG products require greater redundancy to survive the glass fracture when acting as load bearing elements in glass structures [1]. Glass fracture can be caused by many influencing factors, for instance, thermal shock and spontaneous breakage due to nickel sulfide [2]. A simple and straightforward way is to add more glass layers and polymeric interlayers in products with the concept of "sacrificial layer". Thus, multi-layered laminated glass (MLG) products, comprising more than three glass layers and two polymeric interlayers have been increasingly used in glass buildings. In Foraboschi's work, it is shown that the double layered LG cannot achieve the fail-safe design unless it is bonded to one another glass layer and the live loads act upon a sacrificial glass layer. Thus, a triple layered LG system might be the most commonly used solution to introduce only one more sacrificial glass layer [3] when considering the weight and cost.

However, glass materials (even thermally or chemically toughened glass) still exhibit significant vulnerability under impact load [4, 5], e.g., debris hit or blast load. Therefore, the impact resistance should be carefully considered in the design of glass structures. In addition to the fatal blast impact, impacts on the LG element in glass structures are more likely to be the following two types: soft body impact such as human body hit or falling [6-8], or hard body impact like windborne debris impact or armed attack [9, 10]. The structural calculations on the soft body impact to the glass products, e.g. glass balustrade [11], were continuously updated and have reached a high level of accuracy, which can be found in the existing design code and specifications. However, the report concerning hard body impact which shows greater threat to the glass products is still limited so far.

1.2 Laminated glass subjected to hard body impact

Investigations into the hard body impact on the glass products are commonly carried out by laboratory tests requiring great expense or numerical simulation which demands the expertise of designers [12, 13]. In the laboratory tests, small missiles to simulate windborne debris [14-16], large weight impactor with steel hemispherical head to simulate objects falling [17] are frequently used. In the automotive engineering, a headform impactor having aluminium sphere and Polyvinyl chloride (PVC) skin is designed to simulate human head [18-20]. As such headform impactor is covered by a soft PVC skin, its impact feature is more close to that of soft body impact. The impact force/acceleration in headform impact commonly has a smooth peak which is followed by another smooth peak with greater duration and much lower magnitude. The results are without strong oscillation [21]. Wang et al. conducted a series of experiment on testing both the pre- and post-fracture behaviour of square LG panels using ionoplast interlayer [17]. The results show the variation of the energy dissipation feature and the transverse stiffness under impacts with increasing impact velocities. However, the data from the laboratory tests is still limited because they are expensive and cannot cover as many design variables as the numerical models can.

Popular numerical methods such as finite element method (FEM) can be frequently seen in modelling the impact failure of LG products [22, 23]. Majority of the works using FEM focus on developing applicable failure criterion for glass materials [24] or glass-interlayer adhesion interface [25]. Other numerical models such as combined finite-discrete element method (FDEM), which couples the advantage of discrete element method (DEM) in modelling fracturing, fragmentation and that of FEM in modelling polymer behaviour, have also been used in the related topic [7, 8]. It shows that in the numerical attempts, in order to improve the computation accuracy, complex mechanical models were kept being developed and implemented into the numerical model [26, 27]. However, this also brings more difficulties for the engineers to conduct a complex and concise simulation [28]. In the design stage, to have a quick evaluation of the impact resistance of glass products, an analytical model might be more practical for engineers [29]. In particular, it is of significance to have rational prediction of the pre-crack impact response, which is defined as the impact response such as impact force, transverse displacement or associated deformation of glass panels before the initial fracture of glass. The current design code commonly suggests a verification test of impact resistance should be performed on glass products with Type Testing. Several levels of basic impact energy are given to test glass products using steel strikers or balls to simulate hard body impact. Each level corresponds to a certain criterion such as no penetration, no breakage. Once an appropriate analytical model can be developed for MLG under hard body impact, a designer can derive the relationship between basic impact energy and the impact response of MLG. The relationship can be used to get the induced stress in glass which can then be evaluated with the allowable stress criterion.

1.3 Structural calculation on laminated glass

As above mentioned, the structural calculation of the soft body impact on glass products is available in several design codes, e.g. in German standard DIN 18008-4 'Glass in building – design and construction rules – part 4: additional requirements for barrier glazing' [30], soft body impact load is simplified to the equivalent static loads derived from a two-degree-of-freedom model. However, compared to the analytical studies on the impact response of composite laminates which can be frequently found, reports concerning the glass laminates are extremely limited. A recent work of Yuan et al. [19] proposed an analytical model for thin automotive LG subjected to low velocity impact of headform impactor. The first-order shear deformation plate theory incorporating the effect of bending, membrane and transverse shear was introduced. The peak transverse displacement and contact force from analytical model were compared with that from experimental test. Although an evident difference in the contact duration between analytical and experimental results can be seen, the trend of transverse displacement was satisfactory. Other analytical models commonly focus on the static load [31, 32] or blast load [33]. Foraboschi [34] proposed the analytical expression to calculate the nonlinear behaviour of glass elements, which was not properly treated in previous codes, under combined axial and lateral loads. His analytical model can accurately predict the experimental load-deflection curves and ultimate loads and has potentials to be applied to any glass member under same load scenario. Mario et al. [35] developed a single element with fractional viscoelastic properties to accurately predict the polymer response under arbitrary time-varying actions. The analytical model of a MLG beam incorporating the fractional viscoelasticity was then developed.

Differing from the limited works on MLG, a large body of reports can be found concerning the composite laminates made of other materials [36, 37]. Choi et al. [38] developed a modified displacement field of plate theory for carbon/epoxy laminates to consider the effect of in-plane pre-load. The analytical contact force history was compared with that from a pendulum impact test. The results show that as the impact energy increases, the analytical result will present higher difference from the experimental result, indicating the impact velocity or impact energy variation needs to be considered in analytical solution. Singh et al. [39] improved a spring-mass system to represent the contact, shear, bending and membrane stiffness of composite laminates. The comparison between FEM result and analytical result shows that the local indentation at impact point should also be considered in a low velocity impact with large mass impactor. Li et al. [40] combined the Reddy's high-order shear deformation theory and the classical laminate theory to develop an integrated model for calculating the dynamic behaviour of hybrid fibre metal laminates. Dhiraj [41] proposed an improved eight-node quadratic isoparametric plate bending element on basis of refined higher order zigzag theory (HRZT) to evaluate the interlaminar stresses of multi-layered composites. Surrogate-based model was also used to provide the optimization for the impact-resistant design of laminates [42]. Analytical model of other composites such as carbon fibre reinforced plastics (CFRP) [43, 44], functionally graded carbon nanotube-reinforced composite (FG-CNTRC) [45] and laminate comprising polymethyl methacrylate (PMMA) and thermoplastic polyurethane (TPU) [46] under dynamic load can also be found.

However, as shown above, the MLG is produced by laminating multiple glass layers, which might be up to 19 mm (e.g., fully tempered glass) for each glass layer. The first order shear deformation theory, which is frequently used in the existing analytical models, is very likely to be not applicable in MLG product, because the multiple glass-polymer interlaminar deformation is complex. In addition, existing reports indicate that the increase of impact energy might generate greater deviation of analytical result from realistic one. The modification on such influence due to impact energy variation should be considered and cannot be found so far. Hence, in this study, three novelty points are primarily introduced: 1) multi-layered glass laminates with PVB or ionoplast interlayers, which have not been involved in the existing publications with analytical efforts, are experimentally tested; 2) the indentation behaviour which is found to dominant the glass fracture in thick MLG is introduced into the nonlinear analytical model as the first attempt; 3) the third order shear deformation theory is adopted to consider complex interlaminar deformation, which is more appropriate for structural MLG than existing works. Finally, a nonlinear analytical model can then be developed for the thick MLG under hard body impact.

In this study, the pre-crack impact response of thick MLG panels under hard body impact with low velocity was experimentally and analytically investigated. The drop weight impact tests were firstly carried out to record the pre-crack testing data, which were then used to determine a key examined time interval with analysing the failure process via high-speed photos. The analytical model for geometrically nonlinear impact response of MLG panels was proposed using third order shear deformation theory (TSDT) and nonlinearity was introduced in the von-Kármán nonlinear stain-displacement relations. The significance of indentation in determining the glass fracture was considered in this model. A comparison between the analytical and experimental results were subsequently conducted to examine the applicability of the proposed model. It was followed by a parametric study to examine the influence due to the factors such as the number of glass layers, glass thickness and ratio, panel size on the pre-crack impact response.

2. Laboratory tests

In this section, drop weight impact tests were conducted to test MLG panels with double PVB or SG interlayers. The pre-crack impact response from a total number of 73 impact attempts with increasing impact velocity was finally recorded. The recorded data will be used to validate the reliability of analytical results when impact velocity varies.

Additional 12 impact attempts which triggered the glass fracture in each MLG panel were also conducted. The high-speed photos and the recorded impact response were used to identify the failure mode and the key examined time interval of impact response. This work can help determine the key reproduced characteristics that the proposed analytical model needs to achieve.

2.1 Testing apparatus

In this work, the structural glass was assumed to be hit by a large mass impactor such as furniture. The impact case was determined to have a low impact velocity less than 10 $m \cdot s^{-1}$. A drop weight impact test method with a peak drop height of 6 m was adopted. A testing approach characterized by a series of impact attempts with gradually increasing drop heights until glass breakage was adopted. The increment of drop heights was 0.1 m or 0.2 m based on the expected fracture state of glass in next impact. The impact velocity in each impact attempt was recorded, even in the attempts with same drop height. This is because the repeated impact attempts cannot guarantee a same impact velocity as the friction of testing system and man-made errors will result in differences in separate testing cases. All sensors including force sensor and accelerometers were connected to data acquisition units, a sampling frequency of 100 kHz was utilized during the tests.

Design of the impactor: the large mass impactor made of steel was designed to be a 13.5 kg weight with a spherical head radius of 40 mm and a cylindrical body. A ring-shaped integrated circuit piezoelectric (ICP) force sensor was installed between the head and the impactor body to measure the impact force. The force sensor has a sensitivity of 4 pC/N with the response threshold less than 0.01 N. An ICP accelerometer with a sensitivity of 2 pC/(m·s^{-2}) was installed near the impactor head to measure its vertical acceleration (**Fig. 1**). In the impact test, the impactor was dropped inside a transparent guide pipe made of Polymethyl methacrylate (PMMA), which had height scale on it.

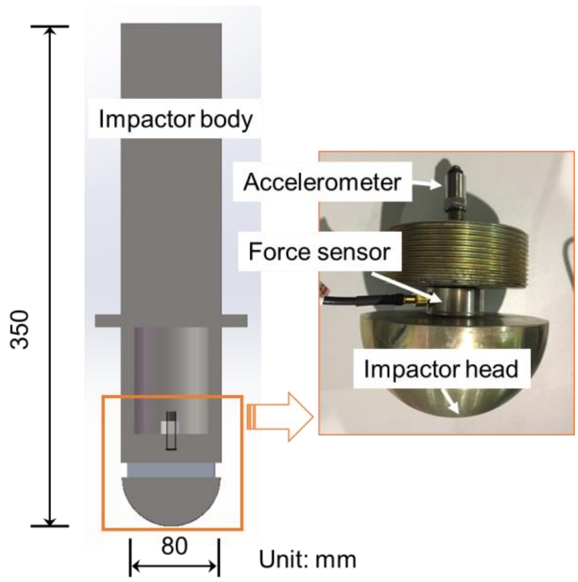

Fig. 1 Configuration and details of impactor

Design of the testing platform: the platform was designed to test specimens with a largest size of 1.5 m × 1.5 m (**Fig. 2 (a)**). A high-speed camera (FASTCAM SA-X2) with two spotlights was adopted via a mirror placed underneath the specimen [47] to capture the exact location of fracture initiation in glass, which can help with defining the mechanical assumption of the analytical model. The frame rate of camera was set as 12500 frames per second. After several trial impact tests, the large mass impact was found to cause too much bouncing and movement of the specimens with simple support. In order to improve the testing accuracy in consecutive impacts, an adjustable upper constraint which only provides very limited rotational stiffness was applied at the specimen edge as shown in **Fig. 2 (b).** The fixing bolts were adjusted to provide very limited rotational constraint at glass edge. A pair of thick neoprene gasket was used to limit the bouncing and movement of the specimen. Through such design, a support condition which was highly close to the simple support can be provided.

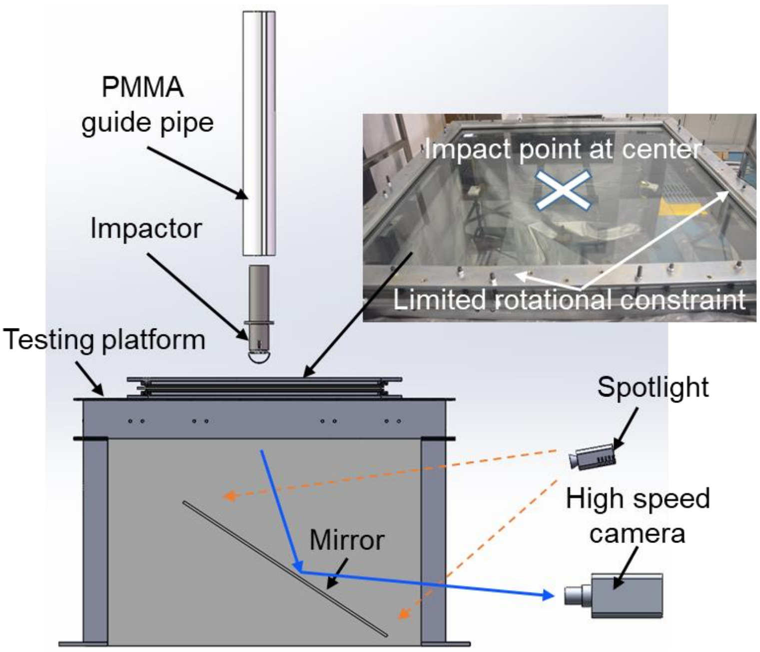

(a)

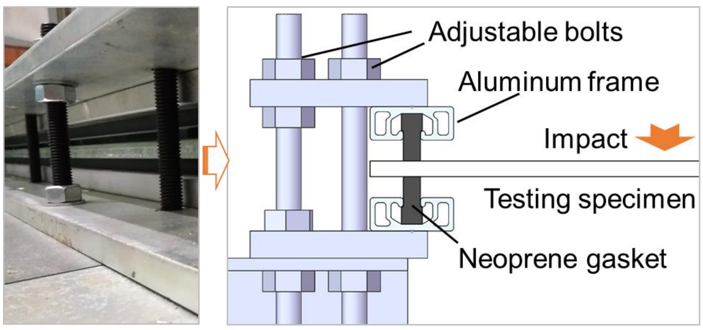

(b)

Fig. 2 Testing platform and details of the support. (a) Testing platform and specimen, the support condition only provides very limited rotational constraint to approximate simple support, (b) details of the support condition.

2.2 Testing specimens

12 MLG panels split into two groups (See **Table 1**) were selected for testing. Fully tempered glass and two popular types of interlayers, PVB (Butacite®) and ionoplast (SentryGlas®, SG) interlayers, were used to make MLG panels. The soda-lime-silica glass products used for the lamination followed the standard requirement of Chinese GB 15763.2 [48]. The glass products had edge treatments including polishing before tempering, and its surfaces did not have any treatment. The MLG products provided by Henan Zhongbo Glass Co., Ltd followed the standard requirement of Chinese GB 15763.3 [49]. The glass lamination adopted a regular roller prelamination process and autoclaving process. Before lamination, interlayers were packed and transported to the manufacturer without exposure to sunlight. The uniaxial tensile property of PVB material was tested at ambient temperature of 20 °C with a loading strain rate of 0.2 s^{-1}. The tangent modulus at original point was found to have a mean value of 73.4 MPa, the mean secant modulus at strain of 0.1 is found to be 13 MPa. The ionoplast interlayer was tested under uniaxial tension at the identical ambient temperature and loading strain rate as well. The tangent modulus at original point was around 535 MPa.

Table 1 Details of the drop weight impact tests

No.	Thermal treatment	Interlayer material	Thickness (mm)	Number of impact attempts	Impact velocity ($m \cdot s^{-1}$)
1-1	Fully tempered	PVB	8/1.52/8/1.52/8	8	0.85 – 1.62
1-2	Fully tempered	PVB	8/1.52/8/1.52/8	13	0.84 – 1.87
1-3	Fully tempered	PVB	8/1.52/8/1.52/8	11	0.85 – 1.73
1-4	Fully tempered	PVB	8/1.52/8/1.52/8	4	0.86 – 1.15
1-5	Fully tempered	PVB	8/1.52/8/1.52/8	8	0.88 – 1.53
1-6	Fully tempered	PVB	8/1.52/8/1.52/8	6	0.79 – 1.34
2-1	Fully tempered	SG	8/3.04/8/3.04/8	1 (N/A)	1.20 (crack)
2-2	Fully tempered	SG	8/3.04/8/3.04/8	6	0.87 – 1.46
2-3	Fully tempered	SG	8/3.04/8/3.04/8	5	0.87 – 1.27
2-4	Fully tempered	SG	8/3.04/8/3.04/8	7	0.96 – 1.23
2-5	Fully tempered	SG	8/3.04/8/3.04/8	4	0.95 – 1.09
2-6	Fully tempered	SG	8/3.04/8/3.04/8	1	1.2

Each specimen had multiple impact attempts before its fracture. The specimens were sized of 1.0 m × 1.0 m. The overlap length of the specimen edges from the support was 15 mm. The peak impact force before glass fracture was found to be 92.4 kN in PVB MLG specimens and 69.4 kN in

SG MLG specimens. The number of impact attempts and corresponding impact velocity interval was collected and shown in **Table 1**.

2.3 Overview of experimental results

Typical impact force variation in pre-crack impact attempt on both PVB MLG and SG MLG specimen is shown in **Fig. 3** (a). PVB MLG ID1-1 and SG MLG ID2-2 were selected to present the results of impact force at a velocity of nearly 1.25 $m \cdot s^{-1}$. It is found that two curves from PVB and SG MLG show high consistency of both their shapes and characteristic values such as peak force and contact duration. The impact force is found to experience two contacts within 6 ms. The durations of each contact are nearly 1.55 ms and 1.73 ms, respectively. The second contact with a much lower peak force will not be the predominant impact hit for cracking the glass, thus it will not be considered in this study. In the first contact (0 - 1.55 ms), the oscillation of the force curve is due to the dynamic coupling effect between the motion of the impactor and glass panel. The coupling effect can be frequently observed in the hard body impact, which is caused by the interaction between the high-frequency deformation behaviour of local glass material near contact point and the impactor movement. It can be seen that the second peak at nearly 0.28 ms and third peak at 0.49 ms are commonly the highest two peaks. The third peak ends at nearly 0.57 ms.

Fig. 3 (b), (c) show the normalized impact force variation of PVB MLG (ID1-1 to ID1-3) and SG MLG (ID2-4 to ID2-6), respectively. Except for ID1-2 in which the fracture initiates from the inner glass layer, the other specimens are found to present initial fracture in the outer glass layer. Through comparing the impact force data and the high-speed photos, the fractures in the tested specimens are found to occur before 0.6 ms, when the third force peak ends. This indicates that the impact response before the third force peak ends is the primary concern in the pre-crack stage.

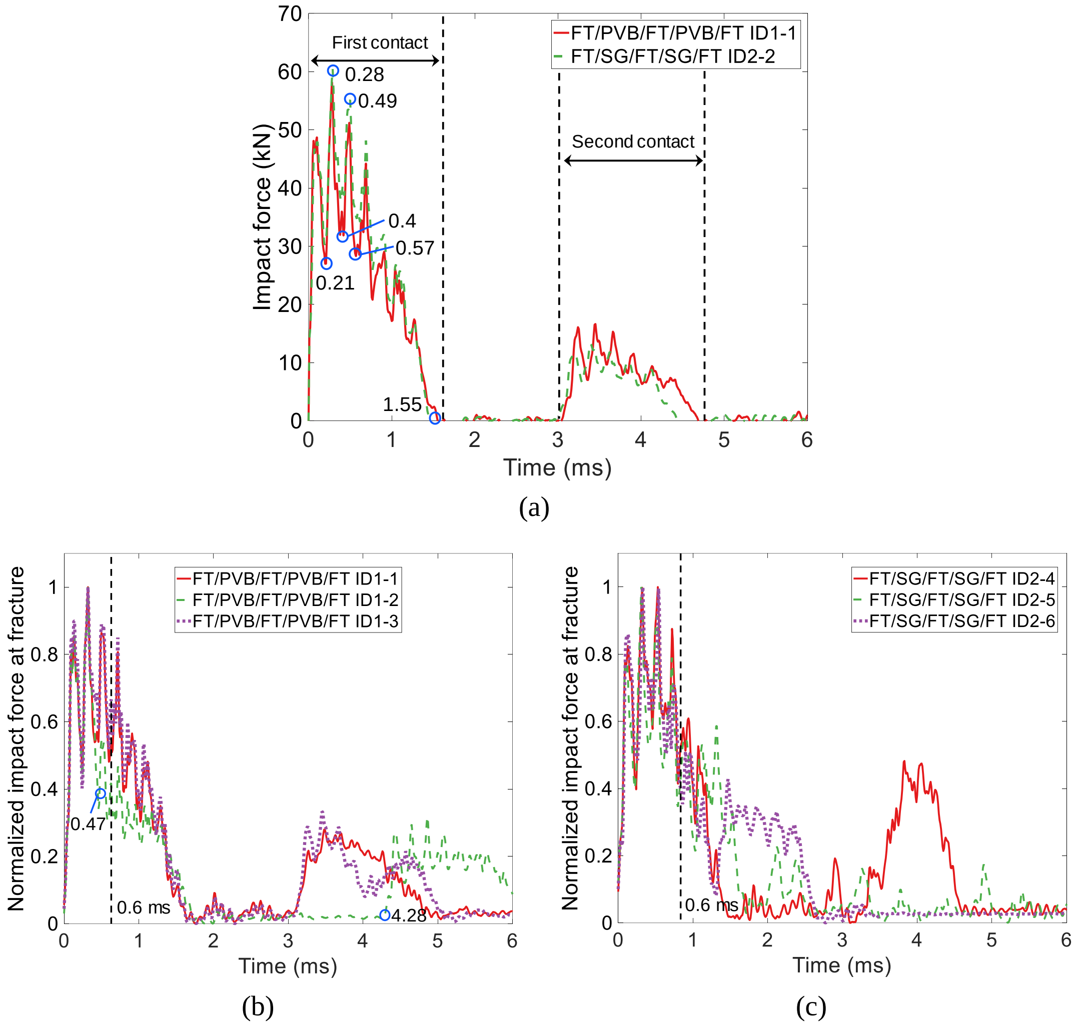

Fig. 3 Typical impact force variation in different impact attempts. (a) Typical impact force variation in pre-crack impact attempt, the numbers refer to the time points of featured peaks or troughs, (b) normalized force at fracture of PVB MLG ID1-1 to ID1-3, the sudden drop of force in ID1-2 occurs at nearly 0.47 ms and the second contact initiates at nearly 4.28 ms, (c) normalized force at fracture of SG MLG ID 2-4 to ID 2-6.

In order to better support the determination of the predominant force peaks and its duration, the high-speed photos at the fracture initiation of PVB MLG ID1-5 and SG MLG ID2-5 are shown in **Fig. 4** (a) and (b), respectively. The fractures in ID1-5 and ID2-5 both initiate at the contact side with the generation of petal shaped fragments near the impact point. Once the cracks propagate beyond the edge of petal shaped fragments, the FT glass fractures into small dices which are similar to that found in the spontaneous breakage (**Fig. 5** (a)). The fracture initiation in the selected specimens is captured at nearly 0.40 – 0.64 ms, which is highly close to the time at force drop from the impact force curves. It is noting that the sampling increment of high-speed camera is 0.08 ms, thus, it might miss precise time of fracture initiation and can only give a time interval.

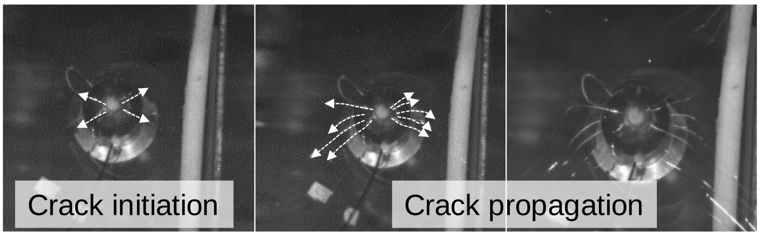

(a)

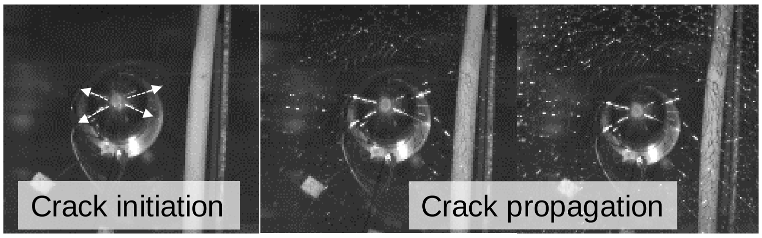

(b)

Fig. 4 High speed photos of crack initiation and propagation in glass at contact side. (a) PVB MLG ID1-5, (b) SG MLG ID2-5.

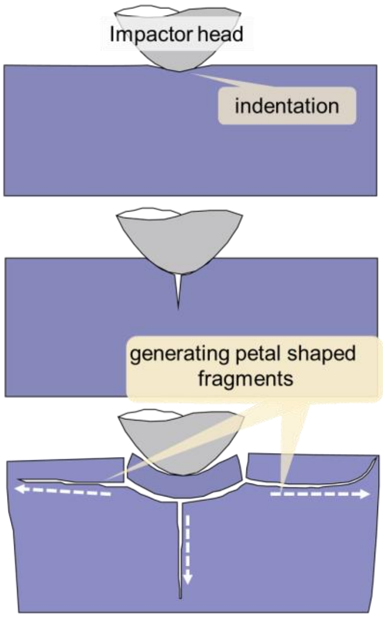

(a) (b)

Fig. 5 Generation of typical fracture pattern caused by indentation process. (a) Typical fracture patterns, i.e. petal shaped fragments near the impact point and small glass dices beyond the edges of petal shapes fragments, (b) generation of fracture pattern, the lateral fractures form the petal shaped fragments.

Through analysing the fracture pattern in **Fig. 5** (a), the fracture initiation and propagation shown in the high speed photos (**Fig. 4**), it is concluded that the glass fracture near the impact point is more likely to be caused by the indentation of the hard impactor head into the glass material. The fracture initiation under hard body impact with low velocity has a similar failure process to that in the indentation failure of thermally tempered glass. The fracture process at the impact point is shown in **Fig. 5** (b). Central crack will propagate vertically beneath the impact point, which is followed by Hertzian cone crack formed in the adjacent area. The lateral cracks will then propagate and generate the petal shaped fragments. Therefore, it is rational to introduce the indentation movement in the theoretical model of hard body impact to consider such failure mode.

2.4 Input energy ratio variation

The impact process always has the loading and unloading (bouncing back of impactor) stage. In the loading stage, the impact force at contact will transform and transfer the kinetic energy of impactor into the LG panel, which finally leads to the fracture of glass. In the above section, it is found the initial impact response before 0.4 - 0.6 ms determines the glass fracture. Therefore, a mean time of 0.5 ms is selected to examine the corresponding input energy ratio α, which is defined as the ratio of the input energy at 0.5 ms to the maximum input energy. The input energy can be easily obtained from the integral of the experimental impact force and displacement. A higher input energy ratio at 0.5 ms commonly refers to the greater efficiency of inputting energy into glass and therefore is more likely to trigger fracture.

ID1-2 and ID1-3 are taken as example to present the variation of input energy ratio with increasing the impact velocity in PVB MLG. The corresponding results are shown in **Fig. 6** (a) and (b), respectively. It can be seen the energy ratio in two specimens is around 0.66 at the lowest impact velocity of nearly 0.84 $m \cdot s^{-1}$ and increases to nearly 0.93 when impact velocity reaches 1.40 $m \cdot s^{-1}$. Once the impact velocity exceeds 1.64 $m \cdot s^{-1}$, the input energy ratio is found to be highly close to 1.0, showing that there is no relative movement between the impactor and glass panel. The result from the impact attempt triggering fracture is also added. It can be seen that in this attempt, the input energy ratio has reached 1.0 before 0.5 ms.

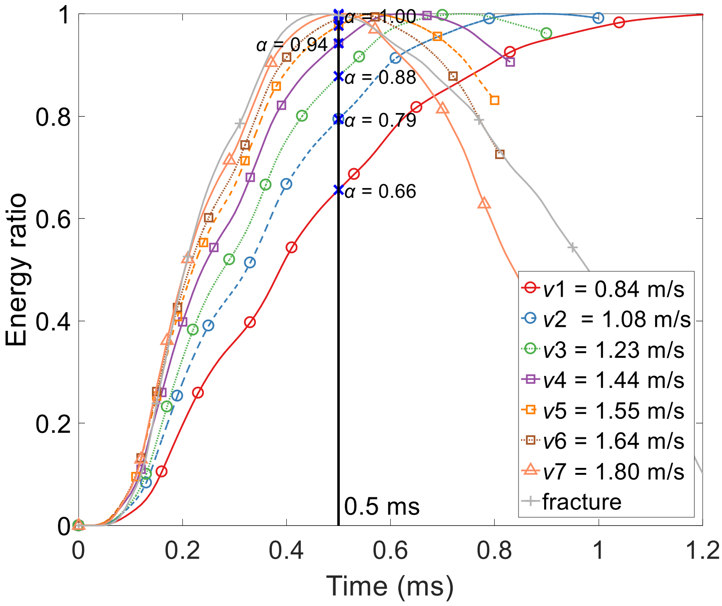

(a)

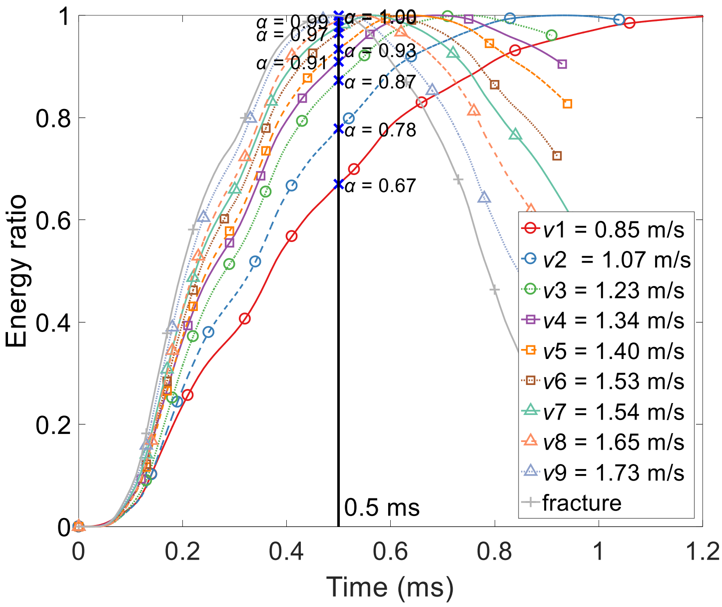

(b)

Fig. 6 Time history of input energy ratio in PVB MLG. (a) PVB MLG ID1-2, α increases from 0.66 to nearly 1.0 when impact velocity varies from 0.84 m·s^{-1} to 1.80 m·s^{-1}, (b) PVB MLG ID1-3, α increases from 0.67 to nearly 1.0 when impact velocity varies from 0.85 m·s^{-1} to 1.73 m·s^{-1}.

In SG MLG group, ID2-2 and ID2-3 are selected to show the time history of input energy ratio. The corresponding results are shown in **Fig. 7** (a) and (b), respectively. The energy ratio in two specimens has a similar value of nearly 0.68 to that in PVB MLG at the lowest impact velocity of nearly 0.87 m·s^{-1}. The energy ratio reaches 0.90 when impact velocity increases to 1.28 m·s^{-1}. The peak energy ratio at 0.5 ms before fracture is found to be 0.95 in ID2-2. The curve from the impact attempt triggering fracture also present an input energy ratio of 0.95 in ID2-2 and 0.93 in ID2-3 at 0.5 ms. In SG MLG, the energy ratio has a delay when comparing with that in PVB MLG and reaches 1.0 at nearly 0.6 ms.

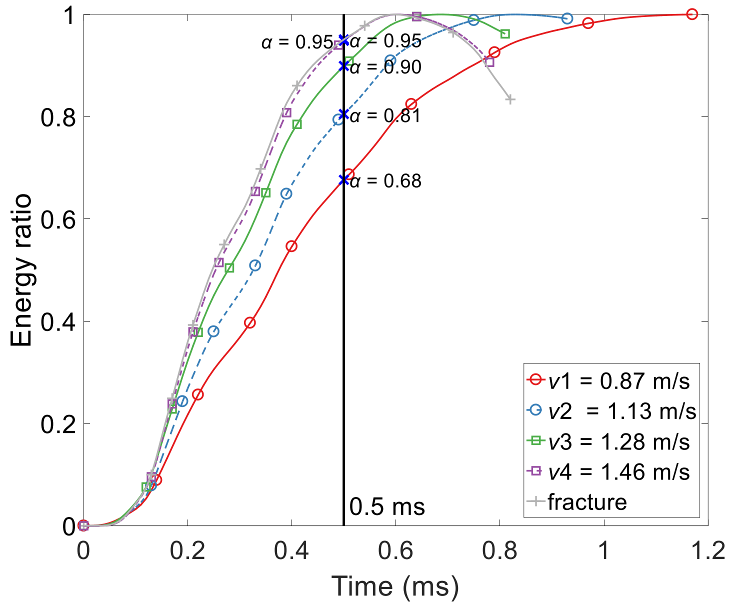

(a)

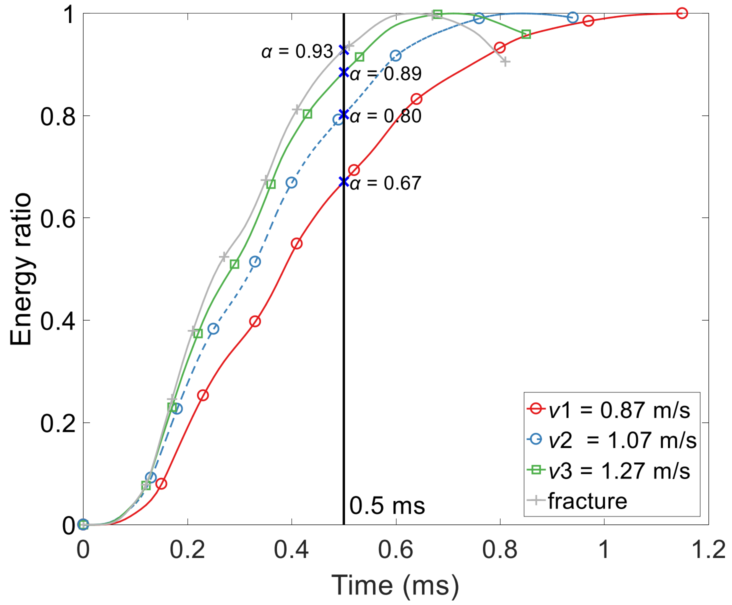

(b)

Fig. 7 Time history of input energy ratio in SG MLG. (a) SG MLG ID2-2, α increases from 0.68 to 0.95 when impact velocity varies from 0.87 $m \cdot s^{-1}$ to 1.46 $m \cdot s^{-1}$, (b) SG MLG ID2-3, α increases from 0.67 to 0.93 when impact velocity varies from 0.87 $m \cdot s^{-1}$ to 1.27 $m \cdot s^{-1}$.

Finally, it can be concluded that the input energy has the trend of being completely transferred to the glass panels within a contact time of 0.5-0.6 ms, when the impact velocity increases and gets closer to the value of triggering fracture. This further confirms that the pre-crack impact response before 0.6 ms should be primarily examined. The lowest transferring ratio is found to be nearly 2/3 of total energy in the examined case before time of 0.5 ms.

3. Nonlinear analytical model

In this section, a low velocity impact (LVI) model applicable to MLG was presented. To simplify the model, the classical Hertz contact law (HCL) was used to characterize the contact behavior between impactor and MLG panel. In the model developed in the current work, the initial velocity of the impactor was determined from combining the HCL and introducing a modified coefficient through experiments.

3.1 Contact model for hard body impact

The general contact laws proposed by Meyer was used extensively to capture the indentation of solids. The contact force, F_c is related to the contact stiffness (K_c) and local indentation (δ(t)) of plate at different loading stages.

At the loading phase,

$$F_C(t)=K_C\left[\delta(t)\right]^r \tag{1}$$

$$K_C=\frac{4}{3}\left(\frac{1-(\mu_{steel})^2}{E_{steel}}+\frac{(\mu_{glass})^2}{E_{glass}}\right)^{-1}\sqrt{R_i} \tag{2}$$

$$\delta(t)=\overline{W}_i(t)-\overline{W}(X,Y,t) \tag{3}$$

where E_{steel}, μ_{steel}, and R_i are the elastic modulus, Poisson's ratio and radius of impactor, respectively (see Sec.4). Here, E_P is the elastic modulus of top layer of MLG. $\overline{W}_i(t)$ and $\overline{W}(X, Y, t)$ represent the displacement of impactor and the deflection of the MLG panel, respectively. For the Hertz's contact law (HCL), which is frequently used in the impact problem [50], r is taken to be 1.5. Studies for Hertzian impact on the composite plate without considering the shear deformation can be found in Ref. [51]. In addition, Abrate [52] found that the HCL was not available to capture the indentation of a sandwich structures with soft core. It is then proposed that the index r should be taken as 0.8 by fitting the experimental results.

At the unloading phase,

$$F_C\left(t\right)=Q_{\max}\left[\frac{\delta\left(t\right)-\delta_0}{\delta_{\max}-\delta_0}\right]^r \tag{4}$$

where Q_{max} and δ_{max} are the maximum contact force and local indentation, respectively. The irrecoverable local indentation δ_0 equals to zero when δ_{max} remains below a critical indentation during loading phase.

Based on the contact law, a simple way was obtained for studying the effect of the various parameters on the impact response of structure. Olsson [53] proposed the closed solution for predicting the contact force and delamination. As we well known, the initial kinetic energy of the impactor is $T= m_i\ V^2/2$. Shivakumar et al. [54] assumed that the energy can be absorbed by the overall deformation of the plate and local indentation. Based on this assumption, the energy balance equation for the plate can be expressed as:

$$\frac{m_i V_0^2}{2}=U_{bs}+U_m+U_c \tag{5}$$

where U_{bs} is the energy associated with the bending and shear deformations and U_m is the energy associated with membrane deformation. The energy U_{bs} and U_m for plates are defined in [53, 54]. For the HCL, the global deformation of plate is ignored and the kinetic energy is related to local indentation by:

$$U_c=\int_0^{\delta_m} F d\delta=\int_0^{\delta_m} K_c\delta^r d\delta=\frac{\left(F_m\right)^{\frac{r+1}{r}}}{\left(r+1\right)\left(K_c\right)^{1/r}} \tag{6}$$

Thus, the maximum contact force F_m can be given

$$F_m=k_c\left(\frac{m_i V_0^2\left(1+r\right)}{2k_c}\right)^{\frac{r}{1+r}} \tag{7}$$

In this work, Hertz’s assumption of impact on a half-space is adopted. The initial velocity of impactor V_0 can be given by introducing the modified coefficient α.

$$V_0=\left(\frac{2k_c\left(F_m/k_c\right)^{\frac{1+r}{r}}}{m_i\left(1+r\right)}\right)^{\frac{1}{2\alpha}} \tag{8}$$

V_0 varies with the maximum contact force F_m obtained by the experiment and the α=0.96 (instead of 1 in HCL).

Hence, the motion equation of impactor is given as follow:

$$m_i\ddot{\overline{W}}_i(t)+F_C(t)=0,\ \overline{W}_i(0)=0,\ \dot{\overline{W}}_i(0)=V_0 \tag{9}$$

where the m_i , $\overline{W}_i(0)$ and $\dot{\overline{W}}_i(0)$ represent the mass, displacement and velocity of the impactor. $\overline{W}_i(0)$ and $\dot{\overline{W}}_i(0)$ are also the initial values of Eq. (9).

3.2 Theoretical formulations

Consider a MLG panel consists three glass layers and two polymeric interlayers which is shown in Fig. 8. The size of the panel is taken as $a\times b$ and the total thickness is h. The XYZ coordinate system is assumed to have its origin located on the middle face of the panels, so that the middle surface lies in the XY-plane. The Z-axis is perpendicular to the XY-plane (Fig. 8). The displacements at a point in the X,Y, and Z directions are $\overline{U}$, $\overline{V}$, and $\overline{W}$, respectively. $\overline{\Psi}_x$ and $\overline{\Psi}_y$ represent the mid-plane rotations of the normal about the Y and X axes.

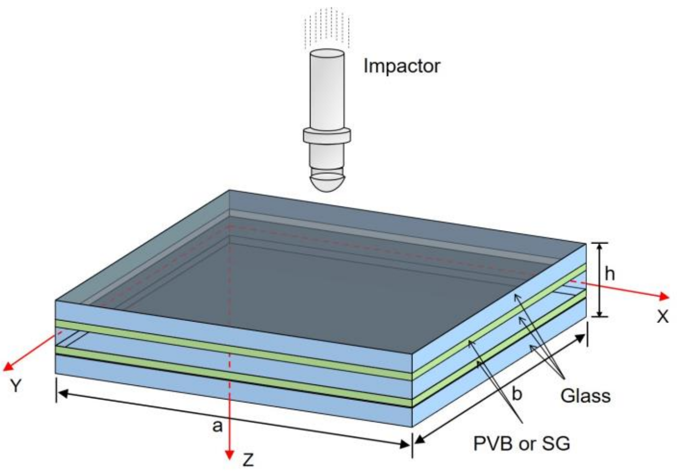

Fig. 8 Schematic of MLG panels loaded by impactor with a spherical head and cylindrical body

The displacement field of MLG panel based on the third-order shear deformation plate theory [55] is expressed as

$$U_1=\overline{U}+Z\left[\overline{\Psi}_x-\chi\frac{4}{3}\left(\frac{Z}{h}\right)^2\left(\overline{\Psi}_x+\frac{\partial\overline{W}}{\partial X}\right)\right],$$

$$U_2=\overline{V}+Z\left[\overline{\Psi}_y-\chi\frac{4}{3}\left(\frac{Z}{h}\right)^2\left(\overline{\Psi}_y+\frac{\partial\overline{W}}{\partial Y}\right)\right],$$

$$U_3=\overline{W},$$

(10)

where χ is a tracer. If χ =1, Eq. (10) corresponds to the case of higher-order shear theory, but when χ=0, Eq. (10) is reduced to the first-order shear plate theory.

The von Kármán strain-displacement relationships of plate associated with the displacement field are

$$\varepsilon_1 = \varepsilon_1^0 + Z\left(\kappa_1^0 + Z^2\kappa_1^2\right), \varepsilon_2 = \varepsilon_2^0 + Z\left(\kappa_2^0 + Z^2\kappa_2^2\right), \varepsilon_3 = 0,$$

$$\varepsilon_4 = \varepsilon_4^0 + Z^2\kappa_4^2, \varepsilon_5 = \varepsilon_5^0 + Z^2\kappa_5^2, \varepsilon_6 = \varepsilon_6^0 + Z\left(\kappa_6^0 + Z^2\kappa_6^2\right), \tag{11}$$

where

$$\varepsilon_1^0 = \frac{\partial \bar{U}}{\partial X} + \frac{1}{2}\left(\frac{\partial \bar{W}}{\partial X}\right)^2, \kappa_1^0 = \frac{\partial \bar{\Psi}_x}{\partial X}, \kappa_1^2 = -\chi\frac{4}{3h^2}\left(\frac{\partial \bar{\Psi}_x}{\partial X} + \frac{\partial^2 \bar{W}}{\partial X^2}\right),$$

$$\varepsilon_2^0 = \frac{\partial \bar{U}}{\partial Y} + \frac{1}{2}\left(\frac{\partial \bar{W}}{\partial Y}\right)^2, \kappa_2^0 = \frac{\partial \bar{\Psi}_y}{\partial Y}, \kappa_2^2 = -\chi\frac{4}{3h^2}\left(\frac{\partial \bar{\Psi}_y}{\partial Y} + \frac{\partial^2 \bar{W}}{\partial Y^2}\right),$$

$$\varepsilon_4^0 = \bar{\Psi}_y + \frac{\partial \bar{W}}{\partial Y}, \varepsilon_5^0 = \bar{\Psi}_x + \frac{\partial \bar{W}}{\partial X}, \varepsilon_6^0 = \frac{\partial \bar{U}}{\partial Y} + \frac{\partial \bar{V}}{\partial X} + \frac{\partial \bar{W}}{\partial X}\frac{\partial \bar{W}}{\partial Y},$$

$$\kappa_4^2 = -\chi\frac{4}{h^2}\left(\bar{\Psi}_y + \frac{\partial \bar{W}}{\partial Y}\right), \kappa_5^2 = -\chi\frac{4}{h^2}\left(\bar{\Psi}_x + \frac{\partial \bar{W}}{\partial X}\right), \kappa_6^0 = \frac{\partial \bar{\Psi}_x}{\partial Y} + \frac{\partial \bar{\Psi}_y}{\partial X},$$

$$\kappa_6^2 = -\chi\frac{4}{3h^2}\left(\frac{\partial \bar{\Psi}_x}{\partial Y} + \frac{\partial \bar{\Psi}_y}{\partial X} + 2\frac{\partial^2 \bar{W}}{\partial X \partial Y}\right), \tag{12}$$

where $(\varepsilon_1^0, \varepsilon_2^0, \varepsilon_3^0)$ are membrane strains, and $(\kappa_1^0, \kappa_2^0, \kappa_3^0)$ are the bending strains, known as the curvatures.

The governing equation of the higher-order plate theory can be derived using the Hamilton's principle:

$$\int_{\bar{t}_1}^{\bar{t}_2} \left(\delta U + \delta V + \delta K\right) d\bar{t} = 0 \tag{13}$$

where δU and δV are the virtual strain energy and virtual wrok done by external forces, respectively. δK is the virtual kinetic energy, and

$$\delta U = \int_\Omega \int_{-h/2}^{h/2} \left(\sigma_i \delta\varepsilon_i\right) dZ dX dY$$

$$= \int_\Omega \left(\bar{N}_i \delta\varepsilon_i^0 + \bar{M}_i \delta\kappa_i^0 + \bar{P}_i \delta\kappa_i^2 \right) dZdXdY \text{ , } (i = 1,2,6)$$

$$\delta V = -\int_\Omega \left[q(X,Y) \delta U_3 \right] dXdY \text{ , } (i = 1,2,6)$$

$$\delta K = \int_\Omega \int_{-h/2}^{h/2} \rho \left(\dot{U}_j \delta \dot{U}_j \right) dZdXdY \text{ , } (i = 1,2,6)$$

(14)

where a superposed dot on a variable indicates differentiation with respect to time. The equations of motion are obtained from Eq. (14) by setting the coefficients of $\delta\bar{U}$, $\delta\bar{V}$, $\delta\bar{W}$, $\delta\bar{\Psi}_x$, and $\delta\bar{\Psi}_y$ in Ω to zero separately:

$$\delta\bar{U} : \frac{\partial \bar{N}_1}{\partial X} + \frac{\partial \bar{N}_6}{\partial Y} = I_1 \frac{\partial^2 \bar{U}}{\partial \bar{t}^2} + \bar{I}_2 \frac{\partial^2 \bar{\Psi}_x}{\partial \bar{t}^2} - \frac{4}{3h^2} I_4 \frac{\partial^3 \bar{W}}{\partial X \partial \bar{t}^2} \text{ ,}$$

$$\delta\bar{V} : \frac{\partial \bar{N}_6}{\partial X} + \frac{\partial \bar{N}_2}{\partial Y} = I_1 \frac{\partial^2 \bar{V}}{\partial \bar{t}^2} + \bar{I}_2 \frac{\partial^2 \bar{\Psi}_y}{\partial \bar{t}^2} - \frac{4}{3h^2} I_4 \frac{\partial^3 \bar{W}}{\partial Y \partial \bar{t}^2} \text{ ,}$$

$$\delta\bar{W} : \frac{\partial \bar{Q}_1}{\partial X} + \frac{\partial \bar{Q}_2}{\partial Y} + \frac{\partial}{\partial X} \left(\bar{N}_1 \frac{\partial \bar{W}}{\partial X} + \bar{N}_6 \frac{\partial \bar{W}}{\partial Y} \right) + \frac{\partial}{\partial Y} \left(\bar{N}_6 \frac{\partial \bar{W}}{\partial X} + \bar{N}_2 \frac{\partial \bar{W}}{\partial Y} \right)$$

$$+ q - \frac{4}{h^2} \left(\frac{\partial \bar{R}_1}{\partial X} + \frac{\partial \bar{R}_2}{\partial Y} \right) + \frac{4}{3h^2} \left(\frac{\partial^2 \bar{P}_1}{\partial X^2} + 2 \frac{\partial^2 \bar{P}_6}{\partial X \partial Y} + \frac{\partial^2 \bar{P}_2}{\partial Y^2} \right)$$

$$= I_1 \frac{\partial^2 \bar{W}}{\partial \bar{t}^2} - \left(\frac{4}{3h^2} \right)^2 I_7 \frac{\partial^2}{\partial \bar{t}^2} \left(\frac{\partial^2 \bar{W}}{\partial X^2} + \frac{\partial^2 \bar{W}}{\partial Y^2} \right)$$

$$+ \frac{4}{3h^2} I_4 \frac{\partial^2}{\partial \bar{t}^2} \left(\frac{\partial \bar{U}}{\partial X} + \frac{\partial \bar{V}}{\partial Y} \right) + \frac{4}{3h^2} \bar{I}_5 \frac{\partial^2}{\partial \bar{t}^2} \left(\frac{\partial \bar{\Psi}_x}{\partial X} + \frac{\partial \bar{\Psi}_y}{\partial Y} \right) \text{,}$$

$$\delta\bar{\Psi}_x : \frac{\partial \bar{M}_1}{\partial X} + \frac{\partial \bar{M}_6}{\partial Y} - \bar{Q}_1 + \frac{4}{h^2} \bar{R}_1 - \frac{4}{3h^2} \left(\frac{\partial \bar{P}_1}{\partial X} + \frac{\partial \bar{P}_6}{\partial Y} \right)$$

$$= \bar{I}_2 \frac{\partial^2 \bar{U}}{\partial \bar{t}^2} + \bar{I}_3 \frac{\partial^2 \bar{\Psi}_x}{\partial \bar{t}^2} - \frac{4}{3h^2} \bar{I}_5 \frac{\partial^3 \bar{W}}{\partial X \partial \bar{t}^2} \text{ ,}$$

$$\delta\bar{\Psi}_y : \frac{\partial \bar{M}_6}{\partial X} + \frac{\partial \bar{M}_2}{\partial Y} - \bar{Q}_2 + \frac{4}{h^2} \bar{R}_2 - \frac{4}{3h^2} \left(\frac{\partial \bar{P}_6}{\partial X} + \frac{\partial \bar{P}_2}{\partial Y} \right)$$

$$= \bar{I}_2 \frac{\partial^2 \bar{V}}{\partial \bar{t}^2} + \bar{I}_3 \frac{\partial^2 \bar{\Psi}_y}{\partial \bar{t}^2} - \frac{4}{3h^2} \bar{I}_5 \frac{\partial^3 \bar{W}}{\partial Y \partial \bar{t}^{-2}} \text{ ,}$$

(15)

where the inertias I_i (i=1, 2, 3,4,5,7) are given in Appendix A. $\bar{N}_i$, $\bar{M}_i$ and $\bar{P}_i$ are the forces, moments and higher order moments, and other symbols are defined as in [56].

In order to facilitate the solution of the equation of motion, Shen [56] presented the generalized von Kármán equation which can be express in terms of a stress function $\bar{F}$, two rotation $\bar{\Psi}_x$ and $\bar{\Psi}_y$ and a transverse $\bar{F}$. In the current work, this generalized von Kármán equation was adopted. The analytical solution is presented for MLG panel undergoing large deflection based on the third order shear deformation theory [55]. In all the cases, the MLG panel is subjected to a dynamic load Q that travels along the Z axis. The motion equations are given as follow:

$$\begin{bmatrix} \tilde{L}_{14}() & -\tilde{L}_{13}() & -\tilde{L}_{12}() & \tilde{L}_{11}() \\ \tilde{L}_{21}() & \tilde{L}_{23}() & \tilde{L}_{22}() & -\tilde{L}_{24}() \\ \tilde{L}_{34}() & -\tilde{L}_{33}() & \tilde{L}_{32}() & \tilde{L}_{31}() \\ \tilde{L}_{44}() & \tilde{L}_{43}() & -\tilde{L}_{42}() & \tilde{L}_{41}() \end{bmatrix} \begin{bmatrix} \bar{F} \\ \bar{\Psi}_y \\ \bar{\Psi}_x \\ \bar{W} \end{bmatrix} = \begin{bmatrix} 1 & \tilde{L}_{17}() & I_8 \dfrac{\partial()}{\partial X} & I_8 \dfrac{\partial()}{\partial Y} \\ 0 & 0 & 0 & 0 \\ 0 & I_9 \dfrac{\partial()}{\partial X} & I_{10} & 0 \\ 0 & I_9 \dfrac{\partial()}{\partial Y} & 0 & I_{10} \end{bmatrix} \begin{bmatrix} Q \\ \ddot{\bar{W}} \\ \ddot{\bar{\Psi}}_x \\ \ddot{\bar{\Psi}}_y \end{bmatrix} + \begin{bmatrix} \tilde{L}(\bar{W},\bar{F}) \\ -\dfrac{1}{2}\tilde{L}(\bar{W},\bar{W}) \\ 0 \\ 0 \end{bmatrix} \tag{16}$$

where the nonlinear operator ($\tilde{L}()$) and the stress function ($\bar{F}$) can be expressed as follow:

$$\tilde{L}(\ ) = \frac{\partial^2}{\partial X^2}\frac{\partial^2}{\partial Y^2} - 2\frac{\partial^2}{\partial X \partial Y}\frac{\partial^2}{\partial X \partial Y} + \frac{\partial^2}{\partial Y^2}\frac{\partial^2}{\partial X^2} \tag{17}$$

$$\bar{N}_x = \frac{\partial^2 \bar{F}}{\partial Y^2},\ \bar{N}_{xy} = \frac{\partial^2 \bar{F}}{\partial X \partial Y},\ \bar{N}_y = \frac{\partial^2 \bar{F}}{\partial X^2} \tag{18}$$

The coefficients S_{ij} and inertias I_i (i=8, 9, 10) are given in Appendix A. The operators ($\tilde{L}_{ij}()$) introduced in the above motion equations are defined from [56].

In this paper, the functions for immovable in-plane boundary conditions (BCs) are given as

at X=0, a:

$$\bar{W} = \bar{\Psi}_y = \bar{M}_x = \bar{P}_x = 0 \tag{19}$$

$$\bar{U} = 0 \tag{20}$$

at Y=0, b:

$$\bar{W} = \bar{\Psi}_x = \bar{M}_y = \bar{P}_y = 0 \tag{21}$$

$$\bar{V} = 0 \tag{22}$$

in which the quantities $(\bar{M}_x, \bar{M}_y)$ denote the flexural moments and $(\bar{P}_x, \bar{P}_y)$ represent the higher order moments given by [55].

The immovable BCs are converted to integral form as given below:

$$\int_0^b \int_0^a \frac{\partial \bar{U}}{\partial X} dX dY = 0 \tag{23}$$

$$\int_0^a \int_0^b \frac{\partial \bar{V}}{\partial Y} dY dX = 0 \tag{24}$$

where,

$$\frac{\partial \bar{U}}{\partial X} = A_{11}^* \frac{\partial^2 \bar{F}}{\partial Y^2} + \left(B_{12}^* - \frac{4E_{12}^*}{3h^2} \right) \frac{\partial \bar{\Psi}_y}{\partial Y} + A_{12}^* \frac{\partial^2 \bar{F}}{\partial X^2} + \left(B_{11}^* - \frac{4E_{11}^*}{3h^2} \right) \frac{\partial \bar{\Psi}_x}{\partial X}$$
$$- \frac{4}{3h^2} \left(E_{21}^* \frac{\partial^2 \bar{W}}{\partial X^2} + E_{22}^* \frac{\partial^2 \bar{W}}{\partial Y^2} \right) - \frac{1}{2} \left(\frac{\partial \bar{W}}{\partial X} \right)^2 \tag{25}$$

$$\frac{\partial \bar{V}}{\partial Y} = A_{22}^* \frac{\partial^2 \bar{F}}{\partial X^2} + A_{12}^* \frac{\partial^2 \bar{F}}{\partial Y^2} + \left(B_{21}^* - \frac{4E_{21}^*}{3h^2} \right) \frac{\partial \bar{\Psi}_x}{\partial X} + \left(B_{22}^* - \frac{4E_{22}^*}{3h^2} \right) \frac{\partial \bar{\Psi}_y}{\partial Y}$$
$$- \frac{4}{3h^2} \left(E_{21}^* \frac{\partial^2 \bar{W}}{\partial X^2} + E_{22}^* \frac{\partial^2 \bar{W}}{\partial Y^2} \right) - \frac{1}{2} \left(\frac{\partial \bar{W}}{\partial X} \right)^2 \tag{26}$$

where the reduced stiffness $(A_{ij}^*,\ B_{ij}^*,\ D_{ij}^*,\ E_{ij}^*,\ F_{ij}^*,\ H_{ij}^*)$ are the functions of the geometry, materials properties, and stacking sequence of the MLG panels as given in Appendix A.

To solve the dynamic equations of MLG panels, a two-step perturbation approach [56] is used. The dynamic equations can be rewritten in the no-dimensional form.

$$\begin{bmatrix} \gamma_{14} L_{14}() & -L_{13}() & -L_{12}() & L_{11}() \\ L_{21}() & \gamma_{24} L_{23}() & \gamma_{24} L_{22}() & -\gamma_{24} L_{24}() \\ \gamma_{14} L_{34}() & -L_{33}() & L_{32}() & L_{31}() \\ \gamma_{14} L_{44}() & L_{43}() & -L_{42}() & L_{41}() \end{bmatrix} \begin{bmatrix} F \\ \Psi_y \\ \Psi_x \\ W \end{bmatrix} = \begin{bmatrix} 1 & L_{17}(\ddot{W}) & \gamma_{80} \frac{\partial()}{\partial x} & \gamma_{80} \beta \frac{\partial()}{\partial y} \\ 0 & 0 & 0 & 0 \\ 0 & \gamma_{90} \frac{\partial()}{\partial x} & \gamma_{10} & 0 \\ 0 & \gamma_{90} \beta \frac{\partial()}{\partial y} & 0 & \gamma_{10} \end{bmatrix} \begin{bmatrix} \lambda_q \\ \ddot{W} \\ \ddot{\Psi}_x \\ \ddot{\Psi}_y \end{bmatrix}$$

$$+\begin{bmatrix} \gamma_{14}\beta^2 L(W,F) \\ -\frac{1}{2}\gamma_{24}\beta^2 L(W,W) \\ 0 \\ 0 \end{bmatrix} \tag{27}$$

It is convenient to introduce dimensionless parameters and nonlinear operator (L()).

$$\left(W,F\right)=\left(\frac{\bar{W}}{[D_{11}^*D_{22}^*A_{11}^*A_{22}^*]^{1/4}},\frac{\bar{F}}{[D_{11}^*D_{22}^*]^{1/2}}\right),\left(x,y,\beta\right)=\left(\pi\frac{X}{a},\pi\frac{Y}{b},\frac{a}{b}\right),t=\frac{\pi\bar{t}}{a}\sqrt{\frac{E_0}{\rho_0}}$$

$$\left(\gamma_5,\gamma_{14},\gamma_{24}\right)=\left(-\frac{A_{12}^*}{A_{22}^*},\sqrt{\frac{D_{22}^*}{D_{11}^*}},\sqrt{\frac{A_{11}^*}{A_{22}^*}}\right),(\gamma_{10},\gamma_{80},\gamma_{90})=(I_{10},I_8,I_9)\frac{E_0}{\rho_0 D_{11}^*}$$

$$\begin{bmatrix} \Psi_x & \Psi_y \\ M_x & P_x \end{bmatrix}=\frac{a}{\pi[A_{11}^*D_{11}^*A_{22}^*D_{22}^*]^{1/4}}\begin{bmatrix} \bar{\Psi}_x & \bar{\Psi}_y \\ \frac{a\bar{M}_x}{D_{11}^*\pi} & \frac{4a\bar{P}_x}{3h^2D_{11}^*\pi} \end{bmatrix},\lambda_q=\frac{a^4Q}{D_{11}^*\pi^4[A_{11}^*D_{11}^*A_{22}^*D_{22}^*]^{1/4}}$$

$$L(\ )=\frac{\partial^2}{\partial X^2}\frac{\partial^2}{\partial Y^2}+\frac{\partial^2}{\partial Y^2}\frac{\partial^2}{\partial X^2}-2\frac{\partial^2}{\partial X\partial Y}\frac{\partial^2}{\partial X\partial Y}. \tag{28}$$

in which $E_0=E_{\text{glass}}$, $\rho_0=\rho_{\text{glass}}$. In Eq. (27), the dimensionless linear operators (L_{ij}()) are defined in [56].

Substitution of dimensionless parameters into Eqs. (19), (21) and (25)-(26) yields:

at x=0, a:

$$W=\Psi_y=M_x=P_x=0 \tag{29}$$

$$\int_0^\pi\int_0^\pi\left[\gamma_{24}^2\beta^2\frac{\partial^2F}{\partial y^2}-\gamma_5\frac{\partial^2F}{\partial x^2}+\gamma_{24}\left(\gamma_{511}\frac{\partial\Psi_x}{\partial x}+\gamma_{223}\beta\frac{\partial\Psi_y}{\partial y}\right)\right.$$
$$\left.-\gamma_{24}\left(\gamma_{244}\beta^2\frac{\partial^2W}{\partial y^2}+\gamma_{611}\frac{\partial^2W}{\partial x^2}\right)-\frac{1}{2}\gamma_{24}\left(\frac{\partial W}{\partial x}\right)^2\right]dxdy=0 \tag{30}$$

at y=0, b:

$$W=\Psi_x=M_y=P_y=0 \tag{31}$$

$$\int_0^\pi\int_0^\pi\left[\frac{\partial^2F}{\partial x^2}-\gamma_5\beta^2\frac{\partial^2F}{\partial y^2}+\gamma_{24}\left(\gamma_{220}\frac{\partial\Psi_x}{\partial x}+\gamma_{522}\beta\frac{\partial\Psi_y}{\partial y}\right)\right.$$

$$-\gamma_{24}\left(\gamma_{240}\frac{\partial^2 W}{\partial x^2}+\gamma_{622}\beta^2\frac{\partial^2 W}{\partial y^2}\right)-\frac{\gamma_{24}\beta^2}{2}\left(\frac{\partial W}{\partial y}\right)^2\Bigg]dxdy=0 \tag{32}$$

with γ_{ijk} given in Shen [56].

3.3 Solutions for the low velocity impact

The solutions for Eq. (27) consist of an additional displacement and rotation terms as a result of the impact loading. The following initial BCs are adopted in the current work:

$$W(x,y,t)|_{t=0}=\Psi_x(x,y,t)|_{t=0}=\Psi_y(x,y,t)|_{t=0}=0,$$

$$\frac{\partial W(x,y,t)}{\partial t}|_{t=0}=\frac{\partial \Psi_x(x,y,t)}{\partial t}|_{t=0}=\frac{\partial \Psi_y(x,y,t)}{\partial t}|_{t=0}=0. \tag{33}$$

$\tau=\varepsilon t$ is introduced to improve perturbation procedure for solving a nonlinear dynamic problem. The solution equations can be expanded as a function with a small perturbation parameter ε^j (j=1, 2, 3, …).

$$\Psi_x(x,y,\tau,\varepsilon)=\sum_{j=1}\varepsilon^j\psi_{xj}(x,y,\tau),\ \Psi_y(x,y,\tau,\varepsilon)=\sum_{j=1}\varepsilon^j\psi_{yj}(x,y,\tau),$$
$$F(x,y,\tau,\varepsilon)=\sum_{j=0}\varepsilon^j f_j(x,y,\tau),\ W(x,y,\tau,\varepsilon)=\sum_{j=1}\varepsilon^j w_j(x,y,\tau),$$
$$\lambda_q(x,y,\tau,\varepsilon)=\sum_{j=1}\varepsilon^j\lambda_j(x,y,\tau) \tag{34}$$

Substituting Eq. (34) into Eq. (27), and collecting terms of the same order of ε, a set of different order perturbation equations is obtained and solved sequentially.

The first order perturbation equations can be expressed as

$O(\varepsilon)$:

$$\begin{bmatrix}\gamma_{14}L_{14}() & -L_{13}() & -L_{12}() & L_{11}() \\ L_{21}() & \gamma_{24}L_{23}() & \gamma_{24}L_{22}() & -\gamma_{24}L_{24}() \\ \gamma_{14}L_{34}() & L_{33}() & L_{32}() & L_{31}() \\ \gamma_{14}L_{44}() & L_{43}() & L_{42}() & L_{41}()\end{bmatrix}\begin{bmatrix}f_1 \\ \psi_{y1} \\ \psi_{x1} \\ w_1\end{bmatrix}=\begin{bmatrix}\gamma_{14}\beta^2 L(w_1,f_0)+\lambda_1 \\ 0 \\ 0 \\ 0\end{bmatrix} \tag{35}$$

Following the perturbation solutions procedure, one assumes the following form of the first term of $w_1(x, y, \tau)$, $\psi_{x1}(x, y, \tau)$, $\psi_{y1}(x, y, \tau)$ that satisfies the simply supported BCs:

$$w_1(x,y,\tau)=A_{11}^{(1)}(\tau)\sin mx\sin ny\,,\ f_1(x,y,\tau)=B_{11}^{(1)}(\tau)\sin mx\sin ny\,,$$

$$\psi_{x1}(x,y,\tau)=C_{11}^{(1)}(\tau)\cos mx\sin ny\,,\psi_{y1}(x,y,\tau)=D_{11}^{(1)}(\tau)\sin mx\cos ny\,,$$

$$\lambda_1(x,y,\tau)=Q_{11}^{(1)}(\tau)\sin mx\sin ny\,. \tag{36}$$

where the terms (m, n) are used to describe the waveform. For immovable BCs, f_0 (x, y)=-$B_{00}^{(0)}$y²/2-$b_{00}^{(0)}$y²/2.

The substitution of Eq. (36) into Eq. (35) yields

$$B_{11}^{(1)}(\tau)=\gamma_{24}\frac{g_{05}}{g_{06}}A_{11}^{(1)}(\tau),C_{11}^{(1)}(\tau)=m\left(\gamma_{14}\gamma_{24}\frac{g_{02}}{g_{00}}\frac{g_{05}}{g_{06}}-\frac{g_{04}}{g_{00}}\right)A_{11}^{(1)}(\tau),$$

$$D_{11}^{(1)}(\tau)=n\beta\left(\gamma_{14}\gamma_{24}\frac{g_{01}}{g_{00}}\frac{g_{05}}{g_{06}}-\frac{g_{03}}{g_{00}}\right)A_{11}^{(1)}(\tau)\,,$$

$$Q_{11}^{(1)}(\tau)=\left[g_{08}+\gamma_{14}\gamma_{24}\frac{g_{05}g_{07}}{g_{06}}-\gamma_{14}\left(\beta^2B_{00}^{(0)}m^2+b_{00}^{(0)}n^2\beta^2\right)\right]A_{11}^{(1)}(\tau)\,. \tag{37}$$

The second-order equation can be written as

$O(\varepsilon^2)$:

$$\begin{bmatrix}\gamma_{14}L_{14}() & -L_{13}() & -L_{12}() & L_{11}()\\ L_{21}() & \gamma_{24}L_{23}() & \gamma_{24}L_{22}() & -\gamma_{24}L_{24}()\\ \gamma_{14}L_{34}() & L_{33}() & L_{32}() & L_{31}()\\ \gamma_{14}L_{44}() & L_{43}() & L_{42}() & L_{41}()\end{bmatrix}\begin{bmatrix}f_2\\ \psi_{y2}\\ \psi_{x2}\\ w_2\end{bmatrix}=\begin{bmatrix}\gamma_{14}\beta^2L(w_2,f_0)+\lambda_2\\ -\frac{1}{2}\gamma_{24}\beta^2L(w_1,w_1)\\ 0\\ 0\end{bmatrix}. \tag{38}$$

The solutions of Eq. **错误!未找到引用源。** are assumed to have the form

$$w_2(x,y,\tau)=0\,,$$

$$f_2(x,y,\tau)=-B_{00}^{(2)}y^2/2-b_{00}^{(2)}x^2/2+B_{20}^{(2)}(\tau)\cos 2mx+B_{02}^{(2)}(\tau)\cos 2ny\,,$$

$$\psi_{x2}(x,y,\tau)=C_{20}^{(2)}(\tau)\sin 2mx,\psi_{y2}(x,y,\tau)=D_{02}^{(2)}(\tau)\sin 2ny\,,$$

$$\lambda_2(x,y,\tau)=Q_{20}^{(2)}(\tau)\cos 2mx+Q_{02}^{(2)}(\tau)\cos 2ny\,. \tag{39}$$

The solutions of Eq. (39) are obtained from the right side of Eq. (38), no need to guess them. By substituting Eq. (39) into Eq. (38), one has

$$B_{20}^{(2)} = \frac{\gamma_{24} n^2 \beta^2}{32 m^2 \gamma_6} \left(A_{11}^{(1)}\right)^2, B_{02}^{(2)} = \frac{\gamma_{24} m^2}{32 n^2 \beta^2 \gamma_7} \left(A_{11}^{(1)}\right)^2,$$

$$C_{20}^{(2)} = -\gamma_{14}\gamma_{220} \frac{8m^3}{\gamma_{31} + 4\gamma_{320} m^2} B_{20}^{(2)}, D_{02}^{(2)} = -\gamma_{14}\gamma_{233} \frac{8n^3\beta^3}{\gamma_{42} + 4\gamma_{432} n^2 \beta^2} B_{02}^{(2)},$$

$$Q_{20}^{(2)} = \frac{1}{2}\gamma_{14}\gamma_{24} m^2 n^2 \beta^2 \left(\frac{\gamma_8}{\gamma_6} + 2\frac{g_{05}}{g_{06}}\right)\left(A_{11}^{(1)}\right)^2, Q_{02}^{(2)} = \frac{1}{2}\gamma_{14}\gamma_{24} m^2 n^2 \beta^2 \left(\frac{\gamma_9}{\gamma_7} + 2\frac{g_{05}}{g_{06}}\right)\left(A_{11}^{(1)}\right)^2 \tag{40}$$

The third-order equations can be written as

$O(\varepsilon^3)$:

$$\begin{bmatrix} \gamma_{14} L_{14}() & -L_{13}() & -L_{12}() & L_{11}() \\ L_{21}() & \gamma_{24} L_{23}() & \gamma_{24} L_{22}() & -\gamma_{24} L_{24}() \\ \gamma_{14} L_{34}() & -L_{33}() & L_{32}() & L_{31}() \\ \gamma_{14} L_{44}() & L_{43}() & -L_{42}() & L_{41}() \end{bmatrix} \begin{bmatrix} f_3 \\ \psi_{y3} \\ \psi_{x3} \\ w_3 \end{bmatrix} = \begin{bmatrix} 1 & L_{17}() & \gamma_{80}\dfrac{\partial()}{\partial x} & \gamma_{80}\beta\dfrac{\partial()}{\partial y} \\ 0 & 0 & 0 & 0 \\ 0 & \gamma_{90}\dfrac{\partial()}{\partial x} & \gamma_{10} & 0 \\ 0 & \gamma_{90}\beta\dfrac{\partial()}{\partial y} & 0 & \gamma_{10} \end{bmatrix} \begin{bmatrix} \lambda_3 \\ \ddot{w} \\ \ddot{\psi}_{x1} \\ \ddot{\psi}_{y1} \end{bmatrix}$$

$$+ \begin{bmatrix} \gamma_{14}\beta^2 L(w_3, f_0) + \gamma_{14}\beta^2 L(w_1, f_2) \\ 0 \\ 0 \\ 0 \end{bmatrix}. \tag{41}$$

It can be found that the dynamic terms be delayed to appear in the third order equation due to introducing *τ=εt.* The solutions of Eq. (41) are assumed as follow:

$$w_3(x, y, \tau) = A_{13}^{(3)}(\tau)\sin mx \sin 3ny + A_{31}^{(3)}(\tau)\sin 3mx \sin ny,$$

$$f_3(x, y, \tau) = B_{13}^{(3)}(\tau)\sin mx \sin 3ny + B_{31}^{(3)}(\tau)\sin 3mx \sin ny + \ddot{B}_{11}^{(3)}(\tau)\sin mx \sin ny$$

$$\psi_{x3}(x, y, \tau) = C_{13}^{(3)}(\tau)\cos mx \sin 3ny + C_{31}^{(3)}(\tau)\cos 3mx \sin ny + \ddot{C}_{11}^{(3)}(\tau)\cos mx \sin ny$$

$$\psi_{y3}(x, y, \tau) = D_{13}^{(3)}(\tau)\sin mx \cos 3ny + D_{31}^{(3)}(\tau)\sin 3mx \cos ny + \ddot{D}_{11}^{(3)}(\tau)\sin mx \cos ny$$

$$\lambda_3(x, y, \tau) = Q_{11}^{(3)}(\tau)\sin mx \sin ny + \ddot{Q}_{11}^{(3)}(\tau)\sin mx \sin ny$$

(42)

The substitution of Eq. (42) into Eq. (41) yields

$$\ddot{B}_{11}^{(3)} = -\gamma_{24}\frac{m^2 G_{23} g_{04}^{*} + n^2\beta^2 G_{24} g_{03}^{*}}{g_{00} g_{06}}\ddot{A}_{11}^{(1)} = -\gamma_{24}\frac{g_{05}^{*}}{g_{06}}\ddot{A}_{11}^{(1)},$$

$$\ddot{C}_{11}^{(3)} = m\left(\frac{g_{04}^{*}}{g_{00}} - \gamma_{14}\gamma_{24}\frac{g_{02} g_{05}^{*}}{g_{00} g_{06}}\right)\ddot{A}_{11}^{(1)}, \ddot{D}_{11}^{(3)} = n\beta\left(\frac{g_{03}^{*}}{g_{00}} - \gamma_{14}\gamma_{24}\frac{g_{01} g_{05}^{*}}{g_{00} g_{06}}\right)\ddot{A}_{11}^{(1)},$$

$$Q_{11}^{(3)} = \frac{\gamma_{14}\gamma_{24}}{16}\left[\frac{m^4}{\gamma_7} + \frac{n^4\beta^4}{\gamma_6} + 2\frac{m^4 + \gamma_{24}^2 n^4\beta^4 + 2\gamma_5 m^2 n^2\beta^2}{\left(\gamma_{24}^2 - \gamma_5^2\right)}\right]\left[A_{10}^{(1)}(\tau)\right]^3,$$

$$\ddot{Q}_{11}^{(3)} = \left(-\gamma_{14}\gamma_{24}\frac{g_{05}^{*} g_{07}}{g_{06}} - g_{08}^{*}\right)\ddot{A}_{11}^{(1)} - \left[\gamma_{170} - \gamma_{171}\left(m^2 + n^2\beta^2\right)\right]\ddot{A}_{11}^{(1)} +$$

$$\gamma_{80}\left(\gamma_{14}\gamma_{24}\frac{g_{05}}{g_{06}}\frac{m^2 g_{02} + n^2\beta^2 g_{01}}{g_{00}} - \frac{m^2 g_{04} + n^2\beta^2 g_{03}}{g_{00}}\right)\ddot{A}_{11}^{(1)}$$

(43)

As a results, the asymptotic solutions obtained for the perturbation equations with order equal to ε=1, 2, 3 are given below:

$$W(x,y,t) = \varepsilon[A_{11}^{(1)}(t)\sin mx \sin ny] + \varepsilon^3[A_{13}^{(3)}(t)\sin mx \sin 3ny$$
$$+ A_{31}^{(3)}(t)\sin 3mx \sin ny] + O(\varepsilon^4), \quad (44)$$

$$\Psi_x(x,y,t) = \varepsilon[C_{11}^{(1)}(t) + \ddot{C}_{11}^{(3)}(t)]\cos mx \sin ny + \varepsilon^2 C_{20}^{(2)}(t)\sin 2mx$$
$$+ \varepsilon^3[C_{13}^{(3)}(t)\cos mx \sin 3ny + C_{31}^{(3)}(t)\cos 3mx \sin ny] + O(\varepsilon^4), \quad (45)$$

$$\Psi_y(x,y,t) = \varepsilon[D_{11}^{(1)}(t) + \ddot{D}_{11}^{(3)}(t)]\sin mx \cos ny + \varepsilon^2 D_{02}^{(2)}(t)\sin 2ny$$
$$+ \varepsilon^3[D_{13}^{(3)}(t)\sin mx \cos 3ny + D_{31}^{(3)}(t)\sin 3mx \cos ny] + O(\varepsilon^4), \quad (46)$$

$$F(x,y,t) = -\left(\frac{B_{00}^{(0)} y^2 + b_{00}^{(0)} x^2}{2}\right) + \varepsilon[B_{11}^{(1)}(t) + \ddot{B}_{11}^{(3)}(t)]\sin mx \sin ny$$
$$+ \varepsilon^2\left(\frac{-B_{00}^{(2)} y^2 - b_{00}^{(2)} x^2}{2} + B_{02}^{(2)}(t)\cos 2ny + B_{20}^{(2)}(t)\cos 2mx\right)$$
$$+ \varepsilon^3[B_{13}^{(3)}(t)\sin mx \sin 3ny + B_{31}^{(3)}(t)\sin 3mx \sin ny] + O(\varepsilon^4), \quad (47)$$

$$\lambda_q(x,y,t) = \varepsilon[g_1 A_{11}^{(1)}(t) + g_4 \ddot{A}_{11}^{(1)}(t)]\sin mx \sin ny$$

$$+(\varepsilon A_{11}^{(1)}(t))^2\left(g_{02}\cos 2ny+g_{20}\cos 2mx\right)\cdot$$

$$+(\varepsilon A_{11}^{(1)}(t))^3 g_3\sin mx\sin ny+O(\varepsilon^4)$$

(48)

Note that in Eq.错误!未找到引用源。-(48) τ is replaced by t. In Eq. (44), $\varepsilon A_{11}^{(1)}(t)$ is considered as the second perturbation parameter which is the function of the deflection, By taking $(x, y)=(\pi/2m, \pi/2n)$, $\varepsilon A_{11}^{(1)}(t)$ can be expressed as:

$$\varepsilon A_{11}^{(1)}(t)=W_m-\Theta_1 W_m^3+\cdots \tag{49}$$

Substituting equation (49) into equation (48) and applying Galerkin procedure, one has

$$g_{40}\frac{d^2(W_m)}{dt^2}+g_{41}(W_m)+g_{42}(W_m)^2+g_{43}(W_m)^3=\bar{\lambda}_q(t) \tag{50}$$

where

$$\bar{\lambda}_q(t)=\frac{4}{\pi^2}\int_0^{\pi}\int_0^{\pi}\lambda_q(x,y,t)\sin mx\sin ny dxdy\cdot \tag{51}$$

When the $\bar{\lambda}_q(t)$=0, the Eq. (50) becomes duffing equation corresponding to the lager amplitude vibration of plate. We take $\bar{\lambda}_q(t)=F_c(t)$ to consider low velocity impact of panel. Therefore, the SODEs of both the MLG panel and the impactor can be rewritten as:

$$g_{40}\frac{d^2(W_m)}{dt^2}+g_{41}(W_m)+g_{42}(W_m)^2+g_{43}(W_m)^3-g_{44}\left[W_i-W_m\right]^r=0 \tag{52}$$

$$\frac{d^2W_i(t)}{dt^2}=-g_{45}\left[W_i-W_m\right]^r \tag{53}$$

Hence, the SODEs with initial value ($W_m(0)=\dot{W}_m(0)=W_i(0)=0, \dot{W}_i(0)=v$) can be solved by employing the RK4 numerical method. g_{40}, g_{41},…et al. are given in Appendix A.

4. Validation and parametric study

In this section, the proposed analytical model was validated with the experimental data from both PVB and SG MLG panels. The peak value and key shape feature of impact force were expected to agree well with the testing data in the key examined time interval. The analytical model was also required to produce very close results of peak impact force to the experimental data when impact velocity varied.

Followed by the validation procedure, a parametric study was conducted to investigate the influence of the number of glass layers, glass thickness and panel size on the pre-crack impact response. The parameters were designed based on the engineering practice to examine the sensitivity of design variables to impact.

4.1 Validation

As above mentioned, a key time interval of 0.6 ms was determined to examine the feature of pre-crack impact response within it. The impact response before 0.6 ms were then examined in the pre-crack stage. From **Fig. 9**, which gives a comparison on the time history of energy ratio and impact force, in the examined time interval, both PVB and SG MLG have three force peaks and can reach an energy ratio of nearly 1.0. The characteristics of impact force including peak value and its shape feature from the proposed analytical model will be validated with those from experimental results. The initial three force peaks will be named as PeakA, PeakB and PeakC (see dashed box in **Fig. 9** (a)), respectively, to better clarify the validation.

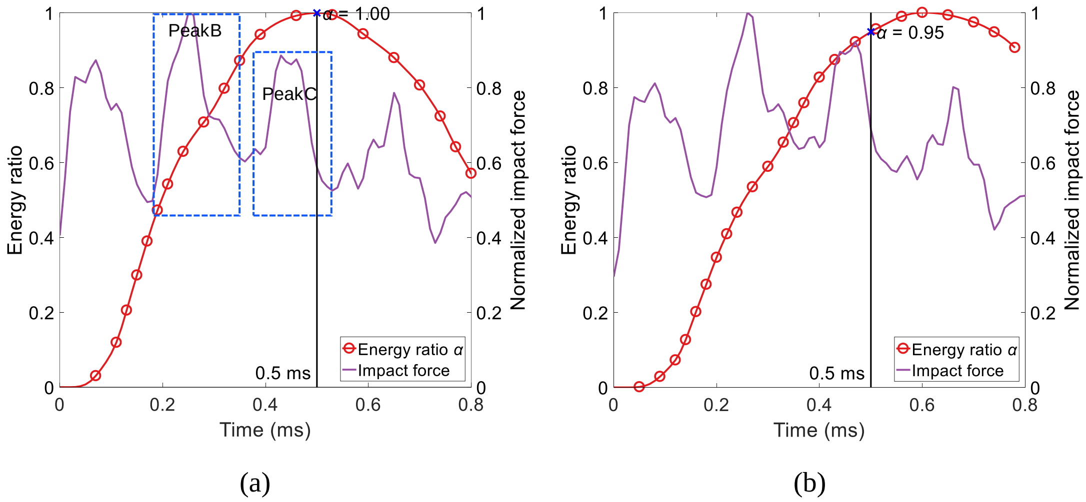

Fig. 9 Normalized impact force and energy ratio variation in the examined time interval. (a) PVB MLG ID1-3, $v = 1.73$ m·s^{-1}, Peaks B and C are determined as key feature to be validated, (b) SG MLG ID2-2, $v = 1.46$ m·s^{-1}.

The material properties used in the validation of pre-crack behavior in MLG panels are as follows: elastic modulus: $E_{\text{glass}} = 70$ GPa, $E_{\text{PVB}} = 267$ MPa, $E_{\text{SG}} = 675$ MPa, $E_{\text{steel}} = 200$ GPa; density: $\rho_{\text{glass}} = 2500$ kg·m^{-3}, $\rho_{\text{PVB}} = 1000$ kg·m^{-3}, $\rho_{\text{SG}} = 1100$ kg·m^{-3}, $\rho_{\text{steel}} = 7960$ kg·m^{-3}; Poisson's ratio: $\mu_{\text{glass}} = 0.22$, $\mu_{\text{PVB}} = 0.45$, $\mu_{\text{SG}} = 0.45$, $\mu_{\text{steel}} = 0.3$. It is noting that, the determination on the elastic modulus of interlayers has considered its dependency on the strain rate, which is around 10^3 s^{-1} from the numerical prediction on the conducted impact attempts. The values of elastic modulus are selected based on the existing report on the material properties of PVB and SG polymers under different strain rates [57, 58]. A sensitivity study is also carried out to examine the influence due to the varying elastic modulus of interlayers (50MPa to 1000 MPa) on the pre-crack impact response. However, the examined variation of elastic modulus only presents negligible influence on the pre-crack impact response. Therefore, it is believed that the adopted material properties are adequate for the validation study.

Considering that the recorded impact velocity of ID1-3 can cover the testing velocity range in PVB MLG specimens, it is taken as the example to validate the result from the proposed model with the experimental data. Four cases from velocity, *v*, of 1.23 $m \cdot s^{-1}$ to 1.73 $m \cdot s^{-1}$ are shown in **Fig. 10** to give a comparison between analytical result and experimental data. From **Fig. 10** (a), it can be seen that the analytical curve grows with a close path to that of PeakB, which initiates from 0.13 ms and reaches its highest value at 0.21 ms. The analytical curve drops at nearly 0.29 ms and it declines with a similar path to that of PeakC as well. The analytical peak can be found at almost the same location of the center (0.31 ms) between PeakB and PeakC, where a trough of experimental value can be found. This trough indicates that the local glass material beneath the impactor head experiences a very short vibration period during the movement of impactor from 0.21 ms (PeakB) to 0.42 ms (PeakC). It hence generates a very fast contact (PeakB), de-contact (trough) and the next contact (PeakC) within this period. If the short vibration of local glass material at contact is removed, the peak instead is very likely to be the same as that in analytical result. In addition, the analytical peak force is 56.0 kN whilst that of experimental result is 57.0 kN in PeakB, showing a good agreement. Thus, it can be concluded that the analytical prediction can achieve the expected result in the examined impact velocity of 1.23 $m \cdot s^{-1}$.

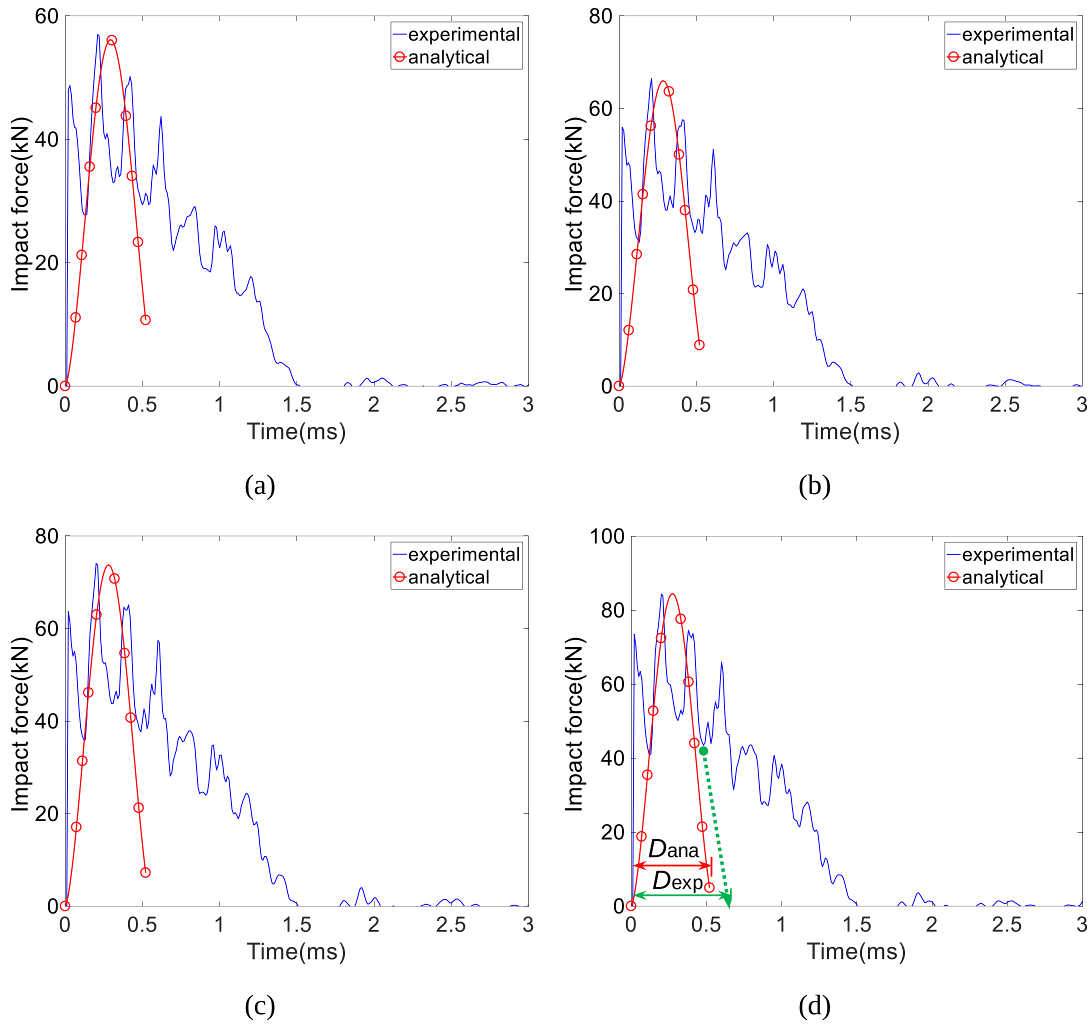

Fig. 10 Validation with the experimental data of selected PVB MLG ID1-3. (a) v = 1.23 m·s^{-1}, (b) v = 1.40 m·s^{-1}, (c) v = 1.54 m·s^{-1}, (d) v = 1.73 m·s^{-1}.

From **Fig. 10** (b) to (d), with the velocity increase the declining path of analytical result has a trend of being slightly deviated from the declining path of experimental PeakC. It shows that the predicted duration (see D_{ana} in **Fig. 10** (d)) is less than the experimental one covered by PeakB and PeakC (see D_{exp} in **Fig. 10** (d)). It is then found that, with the difference of duration, the deviation of predicted peak force from the experimental result decreases from the case of v = 1.23 m·s^{-1} (0.86 kN) to that of v = 1.73 m·s^{-1} (0.14 kN).

ID2-01 is adopted to validate the analytical results of SG MLG. Four cases from the velocity of 0.87 m·s^{-1} to 1.46 m·s^{-1} are shown in **Fig. 11** to give a comparison between analytical result and experimental data. From **Fig. 11** (a), similar to the finding in PVB MLG, it is also seen that the analytical result increases with a close path to the rising part of PeakB. The analytical peak force is 37.9 kN, which is slightly less than that of experimental result in PeakB (38.5 kN), showing a negligible difference. The analytical curve drops at nearly 0.33 ms and its decrease also follows a similar path to the declining part of PeakC. It indicates that the results from proposed model can also map well with the testing data. From **Fig. 11** (b) to (d), it shows that in most cases the predicted duration (see D_{ana} in **Fig. 11** (d)) is consistent with the expected experimental result (see D_{exp} in **Fig. 11** (d)).The maximum absolute difference of peak force is around 0.64 kN in the case of v = 0.87 m·s^{-1}. The difference is relatively small and hence the analytical result can be accepted.

The peak impact force from experimental and analytical results of tested MLG specimens are collected and shown in **Fig. 12**. It is seen that the experimental and analytical peak force have great consistency. It is also concluded that the examined interlayer types will not have much influence on the pre-crack impact force behaviour, the limited difference in the interlayer thickness (1.52 mm and 3.04 mm) also does not have obvious impact on such behaviour.

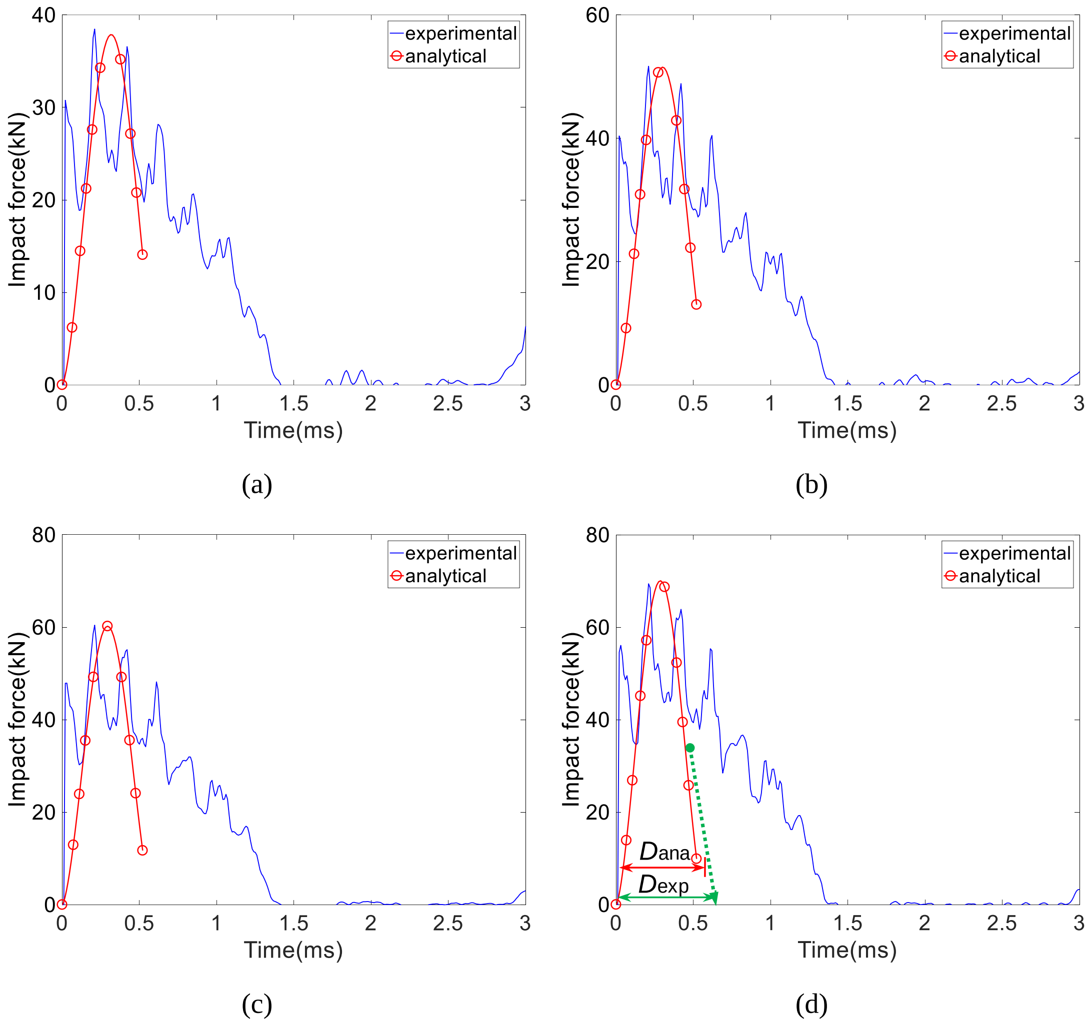

Fig. 11 Validation with the experimental data of selected SG MLG ID2-2. (a) v = 0.87 m·s^{-1}, (b) v = 1.13 m·s^{-1}, (c) v = 1.28 m·s^{-1}, (d) v = 1.46 m·s^{-1}.

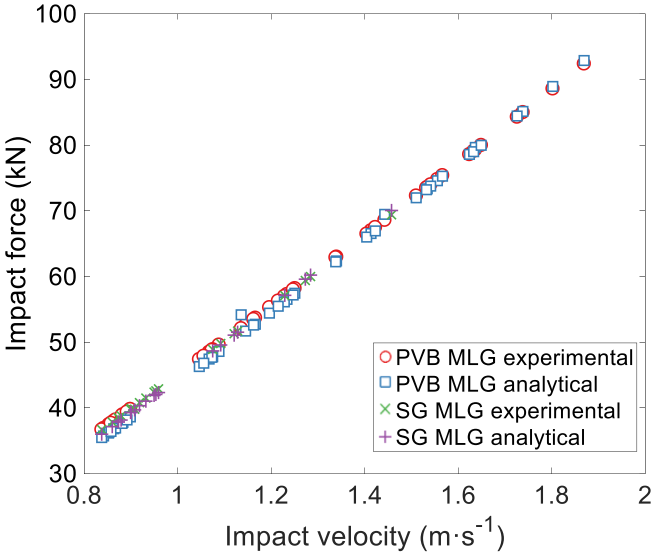

Fig. 12 Comparison of peak impact force from experimental and analytical results

4.2 Parametric study

A parametric study was carried out to examine the effect caused by the factors such as the number of laminated layers, glass thickness and ratio, glass panel size on the pre-crack behaviour of MLG panels. The above study has shown the interlayer types will not show significant influence on the pre-crack behaviour, thus, only SG interlayer was adopted in the following study.

(1) Number of laminated layers

The following three cases are considered to examine the influence due to the number of laminated layers. The impact velocity is set as 1.0 m·s^{-1}.

Case 1-1: glass thickness 8 mm, double glass layers, 1.52 mm SG;

Case 1-2: glass thickness 8 mm, three glass layers, 1.52 mm SG;

Case 1-3: glass thickness 8 mm, five glass layers, 1.52 mm SG.

Fig. 13 shows the time history of impact force, indentation and the relationship of impact force and panel deflection. From the impact force variation in **Fig. 13** (a), the peak force has an increase of 29% from 38.6 kN in Case 1-1 having two glass layers to 49.8 kN in Case 1-3 having five glass layers whilst the maximum indentation slightly increases from 0.19 mm in Case 1-1 to 0.23 mm in Case 1-3. Both the impact force and indentation will drop to zero before 0.7 ms, showing the input energy has reached its peak value within 0.7 ms. Through comparing the maximum value of the indentation (**Fig. 13** (b)) and the panel deflection (**Fig. 13** (c)), it is seen that the indentation (e.g., 0.21 mm in Case 1-2) is much greater than the panel deflection (e.g., nearly 0.013 mm in Case 1-2). This can support the conclusion that the indentation is predominant in the deformation of MLG panels under hard body impact with low velocity. From **Fig. 13** (c), it is seen that the contribution of the panel deflection to the growth of impact force at the impact initiation is much higher than that in the latter stage of impact. The slope of force – deflection curve starts to significantly decrease after the deflection exceeds nearly 0.001 mm. Such slope is close in the examined cases in the latter stage of impact.

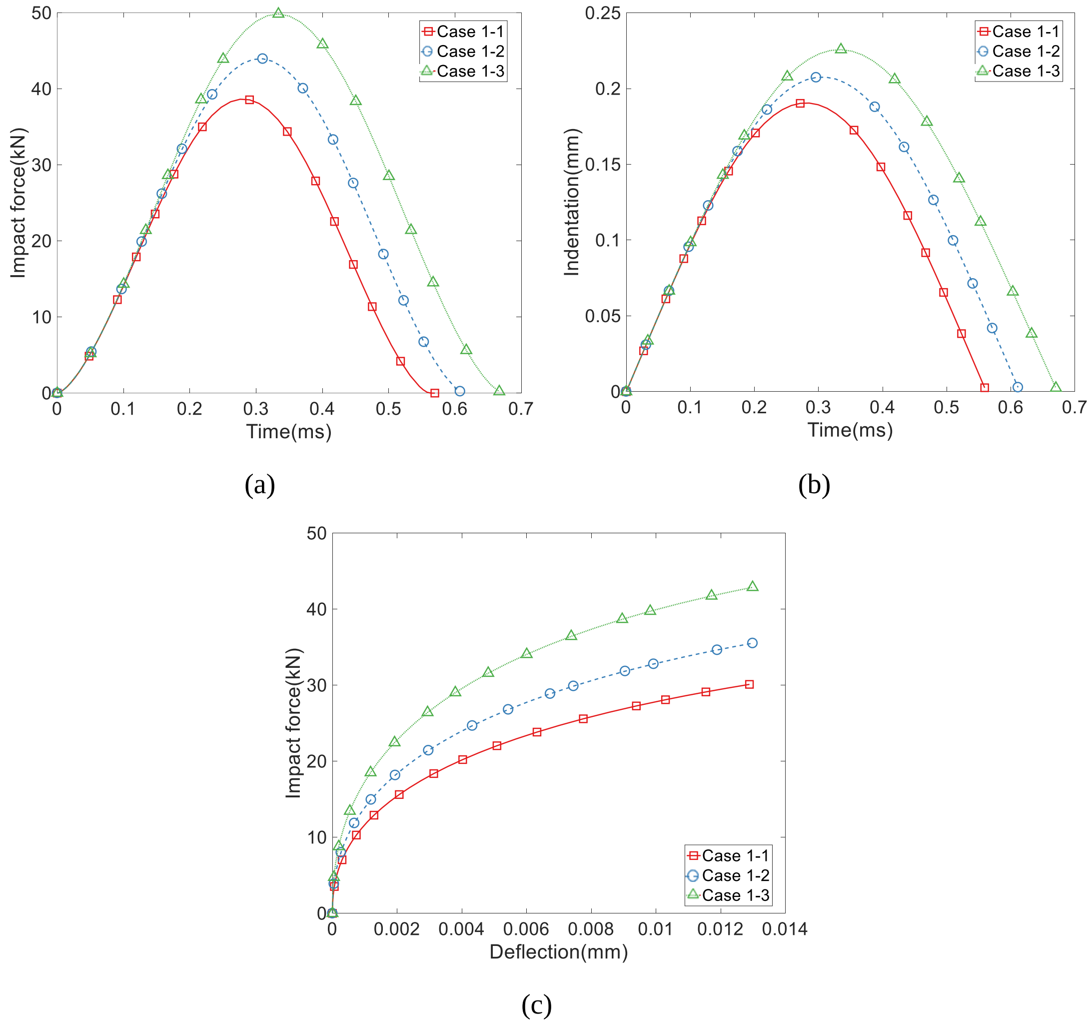

Fig. 13 The effect of the number of laminated layers on the pre-crack behaviour. (a) Impact force, (b) indentation, (c) impact force – panel deflection relationship.

(2) Glass thickness and ratio

The following six cases are considered to examine the influence due to the glass thickness and its thickness ratio. The impact velocity is set as 1.0 m·s^{-1}. The cases are with three glass layers.

Case 2-1: glass thickness 4 mm, three glass layers, 1.52 mm SG;

Case 2-2: glass thickness 8 mm, three glass layers, 1.52 mm SG;

Case 2-3: glass thickness 12 mm, three glass layers, 1.52 mm SG;

Case 2-4: glass thickness 19 mm, three glass layers, 1.52 mm SG;

Case 2-5: glass thickness 4, 8, 12 mm from contact side to opposite side, 1.52 mm SG;

Case 2-6: glass thickness 12, 8, 4 mm from contact side to opposite side, 1.52 mm SG.

It is seen in **Fig. 14** that once the total thickness of glass layers is fixed, the variation of the glass thickness ratio has no obvious influence on the pre-crack behaviour. The given results from Cases 2-5 and 2-6 are consistent with those from Case 2-2, which has a same total glass thickness of 24 mm. From **Fig. 14** (a), the peak impact force increases from 35.7 kN in Case 2-1 to 48.4 kN in Case 2-3 and 53 kN in Case 2-4, the corresponding increase ratio is 35.6% and 48.5%, respectively. The peak indentation increases from 0.181 mm in Case 2-1 to 0.221 mm in Case 2-3 and 0.235 mm in Case 2-4, the corresponding increase ratio is 22.2% and 29.8%, respectively. In order to examine the increase rate of peak impact force and maximum indentation with respect to the increase of total glass thickness, the following equation are given:

$$F_c^{'}=(F_m(h_i)-F_m(h_{ref}))\ /\ (h_i/h_{ref}) \tag{46}$$

where $F_m^{'}$ is the increase rate of peak impact force. F_m is the peak impact force. h_i is the total glass thickness in the examined case. h_{ref} represents the reference total glass thickness of 12 mm. Similarly, the increase rate of peak indentation can be given as follows:

$$\delta_m^{'}=(\delta_m(h_i)-\delta_m(h_{ref}))\ /\ (h_i/h_{ref}) \tag{47}$$

where δ_m is the maximum indentation.

The associated results from cases with different glass thickness, Cases 1-1, 1-3, 2-1, 2-2, 2-3, 2-4, are collected and given in **Fig. 15**. Quadratic polynomials are used to fit the data points. It can be seen that the increase rate of both peak impact force and maximum indentation presents a trend of rising before the thickness of 36 mm and subsequent declining when approaching the thickness of 57 mm. The maximum increase rate of peak impact force is around 4.24 and that of maximum indentation is nearly 0.0134. A high increase rate refers to a high sensitivity of the peak value of impact response to the increase of total glass thickness whilst a plateau of increase rate growth indicates the sensitivity is stable. It can hence be found the sensitivity is high once the total glass thickness exceeds 24 mm.

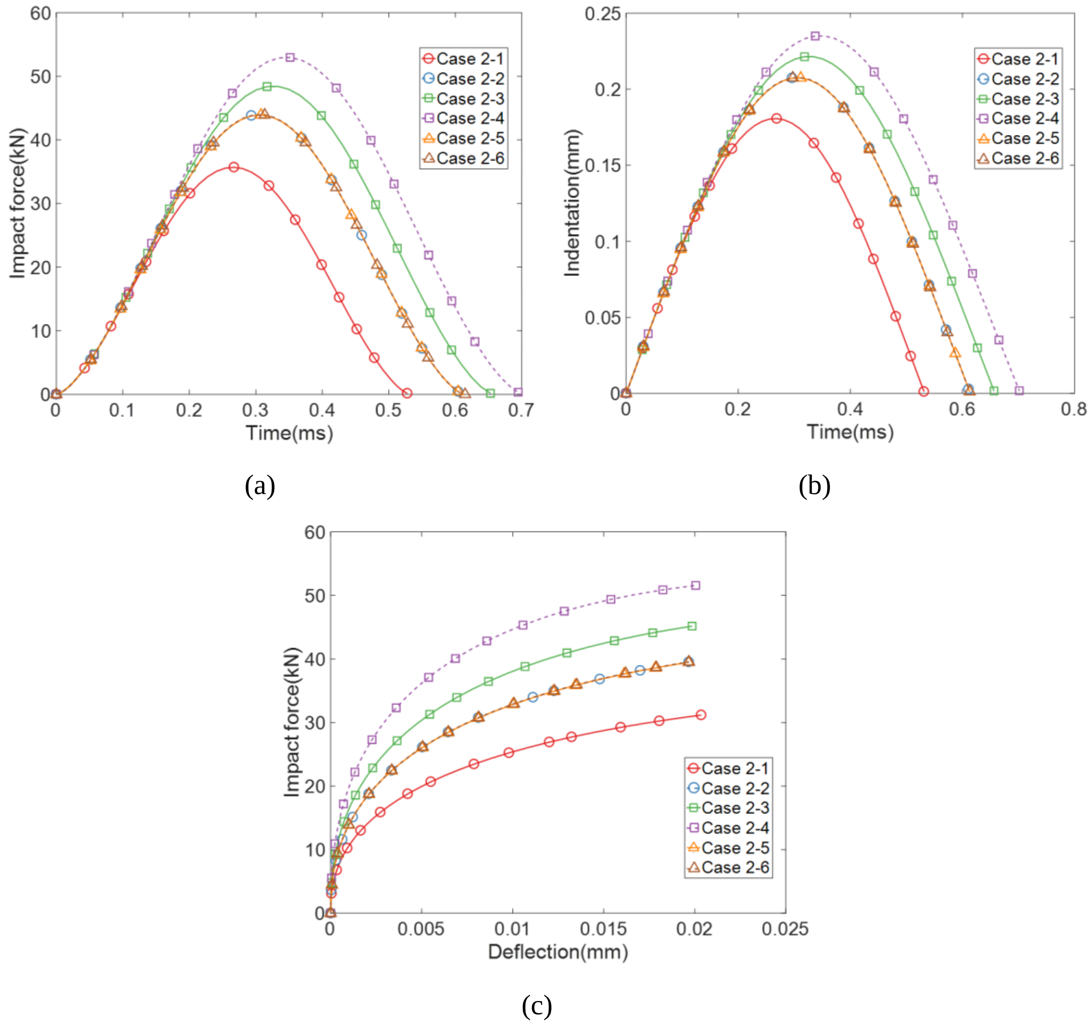

Fig. 14 The effect of the glass thickness and ratio on the pre-crack behaviour. (a) Impact force, (b) indentation, (c) impact force – panel deflection relationship.

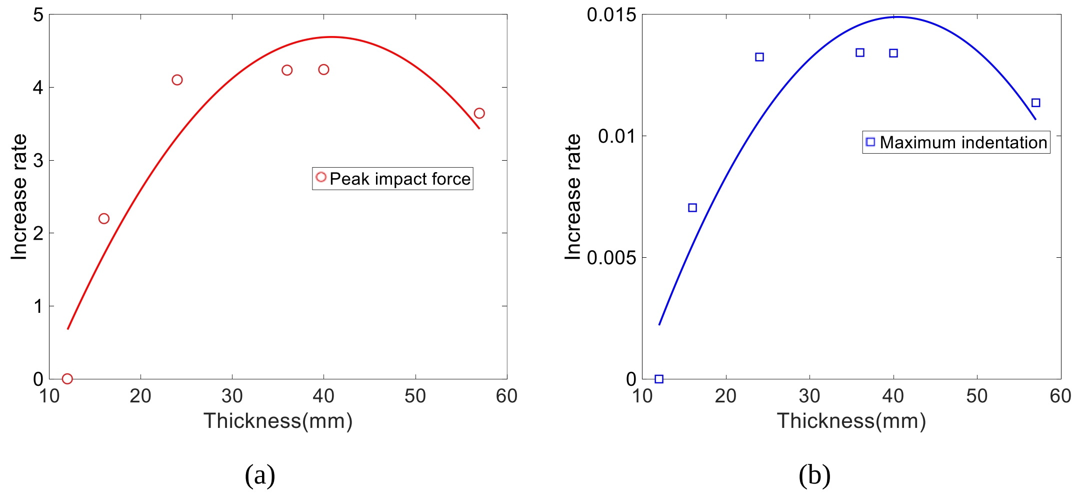

Fig. 15 The increase rate of peak impact force and indentation with varying total glass thickness. (a) Peak impact force, (b) maximum indentation.

(3) Glass panel size

The following three cases are considered to examine the influence due to the glass panel size. The impact velocity is set as 1.0 m·s^{-1}.

Case 3-1: Glass thickness 8 mm, three glass layers, 1.52 m SG, 0.5 m size;

Case 3-2: Glass thickness 8 mm, three glass layers, 1.52 m SG, 1.0 m size;

Case 3-3: Glass thickness 8 mm, three glass layers, 1.52 m SG, 1.5 m size.

From **Fig. 16** (a), it is seen that the peak impact force increases from 26.4 kN in Case 3-1 to 44.0 kN in Case 3-2, 52.4 kN in Case 3-3. The corresponding increase ratio is 67%, 98%, respectively. In **Fig. 16** (b), the maximum indentation increases from 0.148 mm in Case 3-1 to 0.208 mm in Case 3-2, 0.234 mm in Case 3-3 whilst the corresponding increase ratio is 40.5%, 58.1%, respectively. The increase ratio of both peak impact force and indentation is comparatively higher

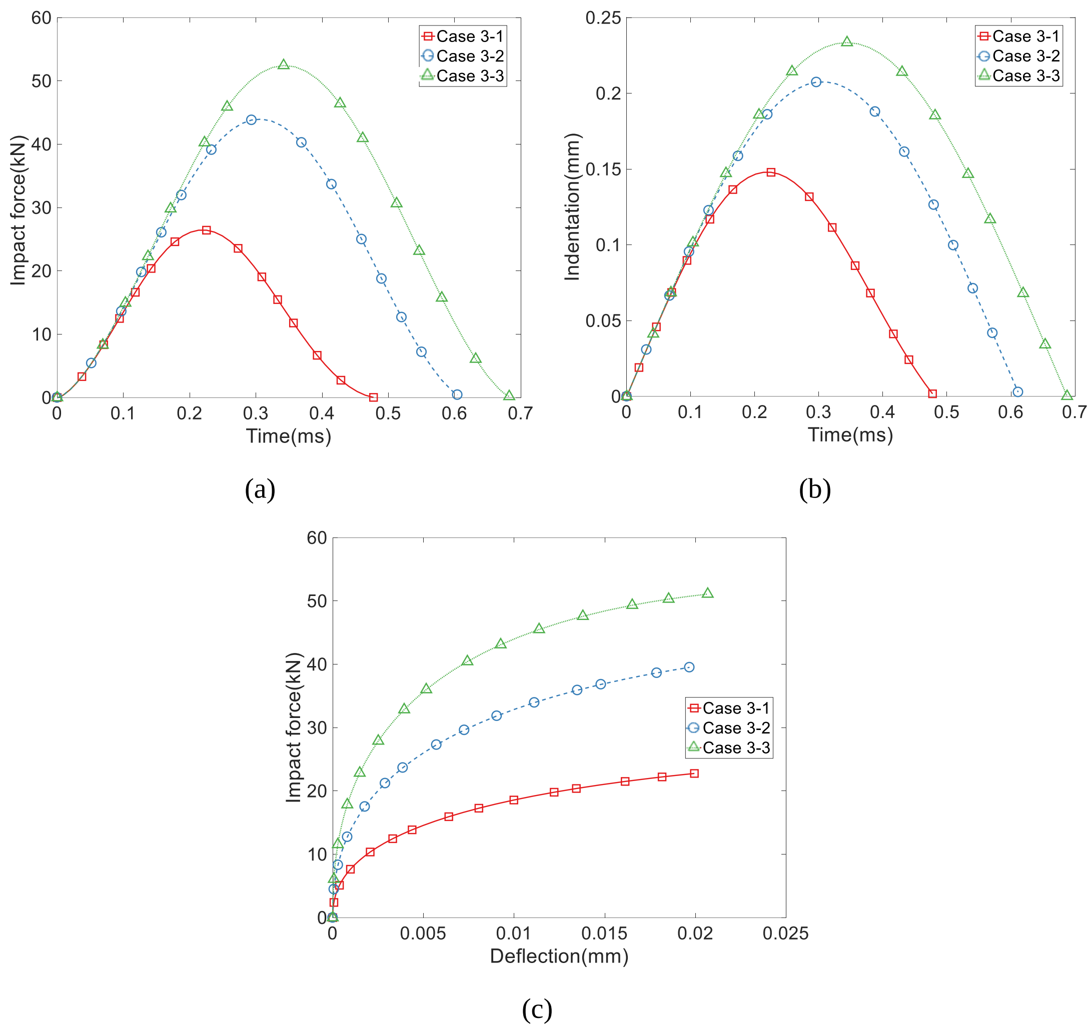

Fig. 16 The effect of the glass panel size on the pre-crack behaviour. (a) Impact force, (b) indentation, (c) impact force – panel deflection relationship.

than that by adjusting the glass thickness, showing the glass panel size is a more significant factor for the pre-crack behaviour. The relationship of impact force and panel deflection also presents great difference by increasing panel size, which can further support this conclusion.

5. Conclusions

This work aims to provide a reliable analytical model for the structural calculation of thick multi-layered laminated glass panels under low-velocity hard body impact. To get rational mechanical assumption from the experiment, the drop weight impact tests using repeated impact attempts were firstly performed on 12 multi-layered PVB or SG laminated glass panels.

There are two key findings which facilitate the development of analytical model from the experimental results:

(1) The evidences from the high-speed photos of glass fracture initiation and the fracture patterns show that the indentation of the hard body impactor into the glass material triggers the glass fracture in the low-velocity hard body impact. The indentation failure is linked to the petal shaped fragments near the impact point and hence can be easily identified.

(2) The key time interval in which the impact response determines the following fracture state of glass is found to be within 0.6 ms. This conclusion is supported by the fracture initiation time from high-speed filming results as well as the finding in analyzing the input energy transferring variation with respect to contact time. It is found that when the impact velocity approaches the value of triggering fracture, the input energy is more likely to be completely transferred into the glass panel within 0.5-0.6 ms.

Therefore, according to the above mentioned two findings from the experimental results, first, the indentation movement was subsequently introduced into the proposed analytical model. Second, as one simplification step of complex dynamic problem, the reproduced key feature of impact response within 0.6 ms by the proposed model was determined to be validated with the experimental results. Finally, a nonlinear analytical model which employed third order shear deformation theory and obtained the solutions of motion equations by a two-step perturbation method was developed. Its applicability was then validated with the testing data and showed satisfactory agreement. The validation procedure also finds that the commonly used interlayer types and thickness will not have much influence on the pre-crack impact force behaviour.

Several factors including the number of glass layers, glass thickness and ratio, panel size were selected to give a parametric study on the associated effects on pre-crack impact response. The following findings can be concluded based on the parametric study:

(1) If the total thickness of glass layers is fixed, the variation of the glass thickness ratio has no influence on the pre-crack behaviour. In the contrast, the increase of peak force and indentation is more sensitive to the increase of total glass thickness after the thickness exceeds 24 mm and presents less sensitivity when the thickness approaches 57 mm.

(2) The panel size is also found to present greater influence on the pre-crack impact response, when comparing with the adjustment of total glass thickness.

Appendix A

In Eqs. (21)-(16), the coefficients I_i (i=1,2,3,4,5,7) are defined by

$$(I_1, I_2, I_3, I_4, I_5, I_7) = \sum_{k=1}^{N} \int_{h_{k-1}}^{h_k} \rho_k (1, Z, Z^2, Z^3, Z^4, Z^6) \mathrm{d}Z \text{ ,} \tag{A.1}$$

and

$$\bar{I}_2 = I_2 - \frac{4I_4}{3h^2}, \quad \bar{I}_3 = I_3 - \frac{8I_5}{3h^2} + \frac{16I_7}{9h^4}, \quad \bar{I}_5 = I_5 - \frac{4I_7}{3h^2}$$

$$I_8 = \frac{I_2\bar{I}_2}{I_1} - \frac{4\bar{I}_5}{3h^2} - \bar{I}_3, \quad I_9 = \frac{4\bar{I}_5}{3h^2} - \frac{4\bar{I}_2 I_4}{3h^2 I_1}, \quad I_{10} = \frac{\left(\bar{I}_2\right)^2}{I_1} - \bar{I}_3 . \tag{A.2}$$

The matrices in the Eqs.(25)-(26) are derived in Shen [59].

$$\begin{bmatrix} \boldsymbol{A}_{ij}^* & \boldsymbol{E}_{ij}^* \\ \boldsymbol{B}_{ij}^* & \boldsymbol{F}_{ij}^* \\ \boldsymbol{D}_{ij}^* & \boldsymbol{H}_{ij}^* \end{bmatrix} = \begin{bmatrix} \boldsymbol{A}_{ij}^{-1} & -\boldsymbol{A}_{ij}^{-1}\boldsymbol{E}_{ij} \\ -\boldsymbol{A}_{ij}^{-1}\boldsymbol{B}_{ij} & \boldsymbol{F}_{ij} - \boldsymbol{E}_{ij}\boldsymbol{A}_{ij}^{-1}\boldsymbol{B}_{ij} \\ \boldsymbol{D}_{ij} - \boldsymbol{B}_{ij}\boldsymbol{A}_{ij}^{-1}\boldsymbol{B}_{ij} & \boldsymbol{H}_{ij} - \boldsymbol{E}_{ij}\boldsymbol{A}_{ij}^{-1}\boldsymbol{E}_{ij} \end{bmatrix}, (i, j\text{=1,2,6}) \tag{A.3}$$

in which $\boldsymbol{A}_{ij}$, $\boldsymbol{B}_{ij}$, $\boldsymbol{D}_{ij}$, etc. are the MLG panels stiffnesses, which are obtained as follow

$$\begin{bmatrix} A_{ij} & B_{ij} & D_{ij} \\ E_{ij} & F_{ij} & H_{ij} \end{bmatrix} = \sum_{k=1}^{N} \int_{h_{k-1}}^{h_k} (\bar{Q}_{ij})_k \begin{bmatrix} 1 & Z & Z^2 \\ Z^3 & Z^4 & Z^6 \end{bmatrix} dZ \quad (i, j = 1,2,6) \tag{A.4}$$

where $\bar{Q}_{ij}$ are the component of the transformed lamina stiffness matrix. For the isotropic materials, $\bar{Q}_{ij}$ are evaluated as follows:

$$\begin{bmatrix} \bar{Q}_{11} & \bar{Q}_{12} & \bar{Q}_{16} \\ \bar{Q}_{22} & \bar{Q}_{26} & \bar{Q}_{66} \\ \bar{Q}_{44} & \bar{Q}_{45} & \bar{Q}_{55} \end{bmatrix}_k = \begin{bmatrix} Q_{11} & Q_{12} & 0 \\ Q_{22} & 0 & Q_{66} \\ Q_{44} & 0 & Q_{55} \end{bmatrix}_k , \tag{A.5}$$

$$\begin{bmatrix} Q_{11} \\ Q_{22} \\ Q_{12} \end{bmatrix}_k = \frac{1}{1-\nu_{12}\nu_{21}} \begin{bmatrix} E_{11} \\ E_{22} \\ \nu_{21}E_{11} \end{bmatrix}_k . \tag{A.6}$$

In Eqs. (52)-(53)

$$g_{40} = -[\gamma_{170} - \gamma_{171}(m^2 + n^2\beta^2)] - g_{08}^* - \gamma_{14}\gamma_{24}\left(\frac{g_{05}^* g_{07}}{g_{06}} - \frac{m^2 g_{02} + n^2\beta^2 g_{01}}{g_{00}} \frac{\gamma_{80} g_{05}}{g_{06}}\right)$$
$$-\gamma_{80}\left(\frac{m^2 g_{04} + n^2\beta^2 g_{03}}{g_{00}}\right), \gamma_{170} = -\frac{I_1 E_0 a^2}{D_{11}^* \pi^2 \rho_0}, \gamma_{171} = \frac{4E_0(I_5 I_1 - I_4 I_2)}{3D_{11}^* h^2 I_1 \rho_0}, \tag{A.7}$$

$$g_{41} = g_{08} + g_{05} g_{07} \frac{\gamma_{14}\gamma_{24}}{g_{06}} , \tag{A.8}$$

$$g_{42} = \frac{-2mn\beta^2\gamma_{14}\gamma_{24}}{3\pi^2}\left(4\frac{g_{05}}{g_{06}} + \frac{\gamma_8}{\gamma_6} + \frac{\gamma_9}{\gamma_7}\right)(1-\cos m\pi)(1-\cos n\pi), \tag{A.9}$$

$$g_{43} = \frac{\gamma_{14}\gamma_{24}}{16}\left(C_{33} + \frac{(n\beta)^4}{\gamma_6} + \frac{m^4}{\gamma_7}\right), C_{33} = 2\frac{m^4 + \gamma_{24}^2 n^4\beta^4 + 2\gamma_5 m^2 n^2\beta^2}{\gamma_{24}^2 - \gamma_5^2} \tag{A.10}$$

$$g_{44} = \frac{4K_c a^2\left(A_{11}^* A_{22}^* D_{11}^* D_{22}^*\right)^{1/8}}{\pi^4 D_{11}^*}\sin\frac{m\pi}{2}\sin\frac{n\pi}{2} \tag{A.11}$$

$$g_{45} = \frac{\rho_0 K_c a^2\left(A_{11}^* A_{22}^* D_{11}^* D_{22}^*\right)^{1/8}}{E_0\pi^2 m^i} \tag{A.12}$$

with the other symbols are given in Shen [56].

Data availability

The data that supports the findings of this study are available within the article.

CRediT authorship contribution statement

Xing-er Wang: Writing – Original Draft, Investigation, Funding acquisition. **Xuhao Huang**: Methodology, Writing – Original Draft, Data curation. **Jian Yang**: Writing – Review & Editing, Supervision, Funding acquisition. **Xiaonan Hou**: Writing – Review & Editing. **Yuhan Zhu**: Software, Formal analysis. **Dongdong Xie**: Validation, Data curation.

Declaration of Competing Interest

The authors declare that they have no known competing financial interests or personal relationships that could have appeared to influence the work reported in this paper.

Acknowledgement

This study was funded by the National Natural Science Foundation of China [Grant No. 51908352, 52078293] and the Shanghai Science and Technology Innovation Action Plan [Grant No. 20dz1201301].

References

[1] Wang X-e, Yang J, Pan Z, Wang F, Meng Y, Zhu Y. Exploratory investigation into the post-fracture model of laminated tempered glass using combined Voronoi-FDEM approach. International Journal of Mechanical Sciences. 2021;190:105989.

[2] Foraboschi P. Analytical modeling to predict thermal shock failure and maximum temperature gradients of a glass panel. Materials & Design. 2017;134:301-19.

[3] Foraboschi P. Optimal design of glass plates loaded transversally. Materials & Design. 2014;62:443-58.

[4] Mohagheghian I, Wang Y, Jiang L, Zhang X, Guo X, Yan Y, et al. Quasi-static bending and low velocity impact performance of monolithic and laminated glass windows employing chemically strengthened glass. European Journal of Mechanics - A/Solids. 2017;63:165-86.

[5] Zhang X, Liu H, Maharaj C, Zheng M, Mohagheghian I, Zhang G, et al. Impact response of laminated glass with varying interlayer materials. International Journal of Impact Engineering. 2020;139:103505.

[6] Zhang X, Hao H, Ma G. Laboratory test and numerical simulation of laminated glass window vulnerability to debris impact. International Journal of Impact Engineering. 2013;55(5):49-62.

[7] Mohagheghian I, Charalambides MN, Wang Y, Jiang L, Zhang X, Yan Y, et al. Effect of the polymer interlayer on the high-velocity soft impact response of laminated glass plates. International Journal of Impact Engineering. 2018;120:150-70.

[8] Mohagheghian I, Wang Y, Zhou J, Yu L, Guo X, Yan Y, et al. Deformation and damage mechanisms of laminated glass windows subjected to high velocity soft impact. International Journal of Solids and Structures. 2017;109:46-62.

[9] Zhang X, Mohammed IK, Zheng M, Wu N, Mohagheghian I, Zhang G, et al. Temperature effects on the low velocity impact response of laminated glass with different types of interlayer materials. International Journal of Impact Engineering. 2019;124:9-22.

[10] Wang X-e, Yang J, Chong WTA, Qiao P, Peng S, Huang X. Post-fracture performance of laminated glass panels under consecutive hard body impacts. Composite Structures. 2020;254:112777.

[11] Kozłowski M. Experimental and numerical assessment of structural behaviour of glass balustrade subjected to soft body impact. Composite Structures. 2019;229:111380.

[12] Wang X-e, Yang J, Liu Q-f, Zhang Y-m, Zhao C. A comparative study of numerical modelling techniques for the fracture of brittle materials with specific reference to glass. Engineering Structures. 2017;152:493-505.

[13] Wang X-e, Yang J, Wang F, Liu Q-f, Xu H. Simulating the impact damage of laminated glass considering mixed mode delamination using FEM/DEM. Composite Structures. 2018;202:1239-52.

[14] Knight CG, Swain MV, Chaudhri MM. Impact of small steel spheres on glass surfaces. Journal of Materials Science. 1977;12(8):1573-86.

[15] Saxe TJ, Behr RA, Minor JE, Kremer PA, Dharani LR. Effects of missile size and glass type on impact resistance of “sacrificial ply” laminated glass. Journal of Architectural Engineering. 2002;8(1):24-39.

[16] Pyttel T, Liebertz H, Cai J. Failure criterion for laminated glass under impact loading and its application in finite element simulation. International Journal of Impact Engineering. 2011;38(4):252-63.

[17] Wang X-e, Yang J, Liu Q, Zhao C. Experimental investigations into SGP laminated glass under low

velocity impact. International Journal of Impact Engineering. 2018;122:91-108.
[18] Liu B, Xu T, Xu X, Wang Y, Sun Y, Li Y. Energy absorption mechanism of polyvinyl butyral laminated windshield subjected to head impact: Experiment and numerical simulations. International Journal of Impact Engineering. 2016;90:26-36.
[19] Yuan Y, Xu C, Xu T, Sun Y, Liu B, Li Y. An analytical model for deformation and damage of rectangular laminated glass under low-velocity impact. Composite Structures. 2017;176:833-43.
[20] Shahriari M, Saeidi Googarchin H. Prediction of vehicle impact speed based on the post-cracking behavior of automotive PVB laminated glass: Analytical modeling and numerical cohesive zone modeling. Engineering Fracture Mechanics. 2020;240:107352.
[21] Wang D, Chen S, Xu W, Zang M. Numerical modelling of impact failure of an automotive windshield glazing subjected to a dummy pedestrian headform. International Journal of Impact Engineering. 2020;141:103564.
[22] Chen S, Mitsume N, Bui TQ, Gao W, Yamada T, Zang M, et al. Development of two intrinsic cohesive zone models for progressive interfacial cracking of laminated composites with matching and non-matching cohesive elements. Composite Structures. 2019;229:111406.
[23] Chen S, Chen H, Mitsume N, Morita N, Bui TQ, Gao W, et al. A nodal-based Lagrange multiplier/cohesive zone approach for dynamic interfacial cracking analysis of thin-walled laminated composite structures. Composite Structures. 2021;256:113112.
[24] Osnes K, Hopperstad OS, Børvik T. Rate dependent fracture of monolithic and laminated glass: Experiments and simulations. Engineering Structures. 2020;212:110516.
[25] Ha YD. An extended ghost interlayer model in peridynamic theory for high-velocity impact fracture of laminated glass structures. Computers & Mathematics with Applications. 2020;80(5):744-61.
[26] Gao W, Liu X, Chen S, Bui TQ, Yoshimura S. A cohesive zone based DE/FE coupling approach for interfacial debonding analysis of laminated glass. Theoretical and Applied Fracture Mechanics. 2020;108:102668.
[27] Solis A, Barbero E, Sánchez-Sáez S. Analysis of damage and interlaminar stresses in laminate plates with interacting holes. International Journal of Mechanical Sciences. 2020;165:105189.
[28] Yan Y, Wiercigroch M. Dynamics of rotary drilling with non-uniformly distributed blades. International Journal of Mechanical Sciences. 2019;160:270-81.
[29] Ma L, Tang Z, Bian Z, Zhu J, Wiercigroch M. Analytical solution for circular inhomogeneous inclusion problems with non-uniform axisymmetric eigenstrain distribution. International Journal of Mechanical Sciences. 2021;194:106213.
[30] Schneider J, Schula S. Simulating soft body impact on glass structures. Proceedings of the Institution of Civil Engineers - Structures and Buildings. 2016;169(6):416-31.
[31] Foraboschi P. Analytical model for laminated-glass plate. Composites Part B: Engineering. 2012;43(5):2094-106.
[32] Galuppi L, Royer-Carfagni G. Analytical approach à la Newmark for curved laminated glass. Composites Part B: Engineering. 2015;76:65-78.
[33] Del Linz P, Liang X, Hooper PA, Wang LZ, Dear JP. An analytical solution for pre-crack behaviour of laminated glass under blast loading. Composite Structures. 2016;144:156-64.
[34] Foraboschi P. Experimental characterization of non-linear behavior of monolithic glass. International Journal of Non-Linear Mechanics. 2014;67:352-70.
[35] Di Paola M, Galuppi L, Royer Carfagni G. Fractional viscoelastic characterization of laminated glass beams under time-varying loading. International Journal of Mechanical Sciences.

2021;196:106274.
[36] Xu K, Chen W, Liu L, Zhao Z, Luo G. A hierarchical multiscale strategy for analyzing the impact response of 3D braided composites. International Journal of Mechanical Sciences. 2021;193:106167.
[37] Yang F, Xie W, Meng S. Global sensitivity analysis of low-velocity impact response of bio-inspired helicoidal laminates. International Journal of Mechanical Sciences. 2020;187:106110.
[38] Choi I-H, Kim I-G, Ahn S-M, Yeom C-H. Analytical and experimental studies on the low-velocity impact response and damage of composite laminates under in-plane loads with structural damping effects. Composites Science and Technology. 2010;70(10):1513-22.
[39] Singh H, Mahajan P. Analytical modeling of low velocity large mass impact on composite plate including damage evolution. Composite Structures. 2016;149:79-92.
[40] Li H, Li Z, Xiao Z, Wang X, Xiong J, Zhou J, et al. Development of an integrated model for prediction of impact and vibration response of hybrid fiber metal laminates with a viscoelastic layer. International Journal of Mechanical Sciences. 2021:106298.
[41] Biswas D, Ray C. Effect of hybridisation in laminated composites on the first ply failure behaviour: Experimental and numerical studies. International Journal of Mechanical Sciences. 2019;161-162:105057.
[42] Tie Y, Hou Y, Li C, Meng L, Sapanathan T, Rachik M. Optimization for maximizing the impact-resistance of patch repaired CFRP laminates using a surrogate-based model. International Journal of Mechanical Sciences. 2020;172:105407.
[43] Baba MN, Dogaru F, Guiman MV. Low velocity impact response of laminate rectangular plates made of carbon fiber reinforced plastics. Procedia Manufacturing. 2020;46:95-102.
[44] Liao B, Zhou J, Li Y, Wang P, Xi L, Gao R, et al. Damage accumulation mechanism of composite laminates subjected to repeated low velocity impacts. International Journal of Mechanical Sciences. 2020;182:105783.
[45] Huang X-H, Yang J, Wang X-E, Azim I. Combined analytical and numerical approach for auxetic FG-CNTRC plate subjected to a sudden load. Engineering with Computers. 2020.
[46] Rühl A, Kolling S, Schneider J. A transparent three-layered laminate composed of poly(methyl methacrylate) and thermoplastic polyurethane subjected to low-velocity impact. International Journal of Impact Engineering. 2020;136:103419.
[47] Van Dam S. Experimental analysis of the Post-Fracture Response of Laminated Glass under Impact and Blast Loading. Ghent: Ghent University; 2017.
[48] Standardization Administration of China. GB 15763.2 Safety glazing materials in building - Part 2: Tempered glass. Beijing: Standards Press of China; 2005.
[49] Standardization Administration of China. GB 15763.3 Safety glazing materials in building - Part 3: Laminated glass. Beijing: Standards Press of China; 2009.
[50] Janda T, Schmidt J, Hála P, Konrád P, Zemanová A, Sovják R, et al. Reduced order models of elastic glass plate under low velocity impact. Computers & Structures. 2021;244:106430.
[51] Olsson R. Impact response of orthotropic composite plates predicted from a one-parameter differential equation. AIAA Journal. 1992;30(6):1587-96.
[52] Abrate S. Localized Impact on Sandwich Structures With Laminated Facings. Applied Mechanics Reviews. 1997;50(2):69-82.
[53] Olsson R. Closed form prediction of peak load and delamination onset under small mass impact. Composite Structures. 2003;59(3):341-9.
[54] Shivakumar KN, Elber W, Illg W. Prediction of Impact Force and Duration Due to Low-Velocity

Impact on Circular Composite Laminates. Journal of Applied Mechanics. 1985;52(3):674-80.
[55] Reddy JN. A simple higher-order theory for laminated composite plates. Journal of Applied Mechanics. 1984;51(4):745-52.
[56] Shen H-S. A two-step perturbation method in nonlinear analysis of beams, plates and shells: John Wiley & Sons; 2013.
[57] Zhang X, Shi Y, Hao H, Cui J. The mechanical properties of ionoplast interlayer material at high strain rates. Materials & Design. 2015;83:387-99.
[58] Xu J, Li Y, Ge D, Liu B, Zhu M. Experimental investigation on constitutive behavior of PVB under impact loading. International Journal of Impact Engineering. 2011;38(2-3):106-14.
[59] Shen H-S. Kármán-type equations for a higher-order shear deformation plate theory and its use in the thermal postbuckling analysis. Applied Mathematics and Mechanics. 1997;18(12):1137-52.